International Journal of Heat and Mass Transfer 52 (2009) 3373–3389

Contents lists available at ScienceDirect

International Journal of Heat and Mass Transfer

journal homepage: www.elsevier.com/locate/ijhmt

Numerical simulation of electromagnetically controlled thermal convection of glass melt in a crucible

C. Giessler, A. Thess *

Department of Mechanical Engineering, TU Ilmenau, P.O. Box 100565, D-98684 Ilmenau, Germany

ARTICLE INFO

Article history:
Received 18 December 2007
Received in revised form 8 October 2008
Available online 18 March 2009

Keywords:
Glass melt
Electromagnetic force
Thermal convection

ABSTRACT

In this paper, we present a three-dimensional numerical study of glass melt in a small scale circular crucible heated by two rod electrodes. Lorentz forces are imposed into the melt by applying an additional external magnetic field. The coupled non-linear conservation equations for mass, momentum, energy and electrical charge are solved with the commercial finite volume code FLUENT. We perform numerical parameter studies by varying the magnetic flux density and the electrode potential to verify the influence of the Lorentz force on the velocity and temperature distribution in the crucible. We observe that the Lorentz force leads to an overall increase of the kinetic energy. Especially below the electrodes, a region which is not affected by buoyancy, the Lorentz force increases the velocity significantly. If the Lorentz force is the dominating driving force the mean velocity is almost a linear function of the Lorentz force. For counteracting Lorentz force and buoyancy between the electrodes we find a discontinuous modification of the flow pattern during the transition from buoyancy dominated to a Lorentz force dominated flow regime and vice versa. Even more, we pass through a hysteresis and obtain two steady solutions for one set of parameters depending on the starting conditions. Furthermore, we identify regimes in which we have a significant improvement of the temperature homogenization. The results show that Lorentz forces provide a new way to influence thermally driven convection of molten glass and can lead to the improvement of mixing.

© 2009 Elsevier Ltd. All rights reserved.

1. Introduction

Over the last decades the need to produce high quality glass has significantly increased, which requires highly homogenous glass melt. Several techniques like electric boosting, mechanical stirring, and bubbling are applied to increase the homogenization rate. Beside the already established mixing techniques one would like to know, if Lorentz forces

$$\mathbf{f_L} = \mathbf{J} \times \mathbf{B}_0,$$

generated by a current density $\mathbf{J}$ and an external magnetic field $\mathbf{B}_0$, can considerably influence the flow and can avoid undesired flow pattern. Especially in melter configurations with electrodes, like in all-electric melting furnaces, forhearts, or feeders and even electric furnaces for high nuclear waste, this technique is of great interest as the magnetic field is provided contactlessly without introducing additional impurities into the melt. The Lorentz force can be considered as a global force because it is acting in all regions of the melt where $\mathbf{J}$ and $\mathbf{B}_0$ are non-zero. But in order to create sufficient large magnetic fields the dimensions of the device should be small. While the application of electromagnetic forces for flow control in other areas of material processing like steel casting and production of aluminum is well established [7], the application of electromagnetic forces in glass melts is a comparable new topic. The difficulty with glass melts arises from the fact that their electrical conductivity is nearly five orders of magnitude smaller than that of liquid metals. The goal of the presented work is to model numerically the influence of Lorentz forces in glass melt in a three-dimensional crucible configuration which includes the steady Navier–Stokes equation, the Energy equation and the Laplace equation for the electric potential. It allows us to investigate systematically how varying electrode potentials and magnetic flux densities influence the electromagnetically controlled flow of glass melts, and how strong a electromagnetic force ought to be to achieve significant effects. The presented numerical study with the commercial software FLUENT should be considered as a first step towards a better understanding of electroprocessing of molten glass as it is performed for a laboratory scale configuration and as it neglects internal heat transfer by radiation.

Methods to use imposed Lorentz forces for homogenization of glass melt were first patented by Walkden in [40]. Without giving technical details, he suggested different arrangements in feeders and furnaces and recognized that the method allows for the production of a variety of different glass flow pattern. Later, various patent applications suggested the use of Lorentz forces for

* Corresponding author. Tel.: +49 3677 692445.
E-mail addresses: cornelia.giessler@tu-ilmenau.de (C. Giessler), thess@tu-ilmenau.de (A. Thess).

0017-9310/$ - see front matter © 2009 Elsevier Ltd. All rights reserved.
doi:10.1016/j.ijheatmasstransfer.2009.01.004

Nomenclature

A	viscosity parameter
B	viscosity parameter
Br	Brinkman number
$\mathbf{B}_0$	magnetic flux density
c_P	heat capacity
D	diameter
$\mathbf{D}$	symmetric stretching tensor
E	conductivity parameter
$\mathbf{f_b}$	gravitational force
$\mathbf{f_L}$	Lorentz force
g	interpolation formula
$\mathbf{g}$	acceleration of gravity
Gr	Grashof number
h	heat transfer coefficient
H	filling level
Ha	Hartmann number
$\mathbf{J}$	electric current density
Nu	Nusselt number
p	pressure
Pr	Prandtl number
R	radius
Ra	Rayleigh number
T	temperature
$\mathbf{u}$	velocity field
U_E	electric potential difference
x,y,z	Cartesian coordinates
α	maximum stretching function
β	thermal expansion coefficient
ϵ	emissivity
η	viscosity
λ	heat conductivity
ϕ	electric potential
ρ	density
σ	electrical conductivity
σ_{sb}	Stefan–Boltzmann constant

Subscripts

0	measured for $B_0 = 0$ T
max	maximum
min	minimum
air	air

homogenization [27,30,15] and for the flow control of glass melts in forehearts and feeders [25]. In [29] Osmanis showed experimentally the influence of electromagnetic stirring on the glass quality and first mentioned the dimensions of the presented laboratory scale setup. This concept of electromagnetic control of buoyant driven convection in a small scale crucible was later taken up by Krieger and co-workers. They have proven the existence of the imposed Lorentz forces in glass melt on the basis of temperature measurements [17,20], stria formation in stacked melts using colored and colorless glass, and calculated the velocities on the basis of cross-correlation of temperature fluctuations [21]. Analytical one-dimensional models of molten glass in electromagnetically controlled pipe flow [12] and electromagnetically controlled thermal convection in a closed loop [13,14] give the mean velocity and temperature distribution as a function of the imposed Lorentz force. They allow extensive parameter studies and can provide a good understanding of the underlying basic physical mechanism. But neither the analytical modeling nor the experiments can give an answer to the following questions: how is the transition from a purely buoyant driven flow to a mainly Lorentz force driven flow characterized and how are the flow pattern and temperature distribution influenced by the Lorentz force? Does the velocity depend linearly on the Lorentz force in a three-dimensional configuration as predicted by the one-dimensional analytical models? The presented paper will give answers to these questions with three-dimensional numerical simulations of a laboratory scale setup which was used in the experimental studies of [20].

Recently, the setup was studied numerically by Cepite and co-workers in [2]. The only objective of this work is to reflect the experimental data without systematic variation of the Lorentz force magnitude. Furthermore, papers on mathematical modeling of electric furnaces are relevant for our numerical studies, which number is limited. In his pioneering work Curran [6] studied the effects of different electrode configurations in a two-dimensional model followed by Austin and Bourne [1] and Mardorf and Woelk [26] who included a feeding rate of the batch. Chen and Goodson [3] presented three-dimensional results assuming constant material properties except in the buoyancy term. Between 1986 and 1988 some papers about three-dimensional simulations of industrial all-electric furnaces were published, which focused on the arrangement and orientation of multiple electrodes and include the pull rate of the batch and the temperature-dependent material properties [4,5,37–39]. Due to the limited computational power at that time the grid refinement was extremely limited. With combined experimental and three-dimensional numerics Hiemjima et al. [16] studied the possibility to control the glass convection with various electric boosting conditions, heat loss through the walls and the charged glass batch.

The paper is organized as follows. In the next section we formulate the considered problem and in Section 3 we describe the implementation of the numerical model. It includes a detailed description of the mesh analysis. After that, we study the results in Section 4. In the first part of Section 4 the Lorentz force distribution is explained followed by a detailed discussion of the velocity and temperature distribution for various parameter settings. The section closes with some global analysis of the results. Finally, we summarize the key results of the work and give some concluding remarks in Section 5.

2. Formulation of the problem

The present approach is to study the electromagnetically controlled thermal convection of glass melt in a small scale cylindrical crucible. The inner radius of the laboratory crucible is $R = 0.04$ m and the fill level of the molten glass is $H = 0.08$ m. Two rod electrodes with a diameter of $D = 0.013$ m are symmetrically immersed 0.06 m into the melt from the top at $(x,y) = (-0.0165\text{ m},0\text{ m})$ and at $(x,y) = (0.0165\text{ m},0\text{ m})$, see Fig. 1. The prescribed setup has two symmetry planes, namely the plane $x = 0$ m and the plane $y = 0$ m which are shown in Fig. 2.

The glass melt is assumed to be Newtonian with a constant heat capacity c_P and the viscosity $\eta(T)$ and the electrical conductivity $\sigma(T)$ being exponential functions of the temperature T. The viscosity is a decreasing function of the temperature and can be approximated by the Vogel–Fulcher–Tammann equation

$$\eta(T) = \eta_0 \exp\left(\frac{A}{T+B}\right), \tag{1}$$

with the constants η_0, A and B depending on the specific glass [28]. The electrical conductivity increases with temperature and can be expressed by the Rasch–Hinrichsen equation [28]

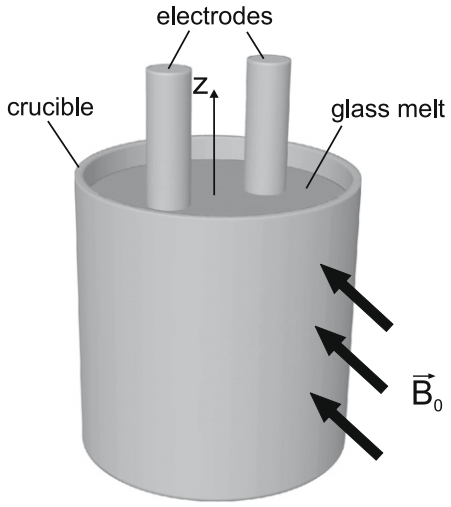

Fig. 1. Sketch of the considered problem.

$$\sigma(T) = \sigma_0 \exp\left(-\frac{E}{T}\right). \tag{2}$$

Again the constants σ_0, E and F depend on the glass type. Furthermore, the density $\varrho(T)$ is assumed to be a linear function of temperature and the heat conductivity $\lambda(T)$ is approximated by a quadratic function of temperature. The basis for the functional description of $\rho(T)$ and $\lambda(T)$ are experimental measurements of both quantities for the considered composition.

Between the electrodes a constant electric potential difference U_E is applied. As a result we obtain a current density distribution $\mathbf{J}$ which is heating the melt due to the Joule effect with the volumetric heat input J^2/σ. As we have heat losses at the surface and the crucible walls, temperature and density gradients develop in the melt. Thus, with the acceleration of gravity $\mathbf{g} = g\mathbf{e_z}$, the gravitational force

$$\mathbf{f_b} = \varrho g \mathbf{e_z},$$

leads to buoyancy which is driving the flow. Such buoyant driven convection is the basis of so-called all-electric furnaces and already

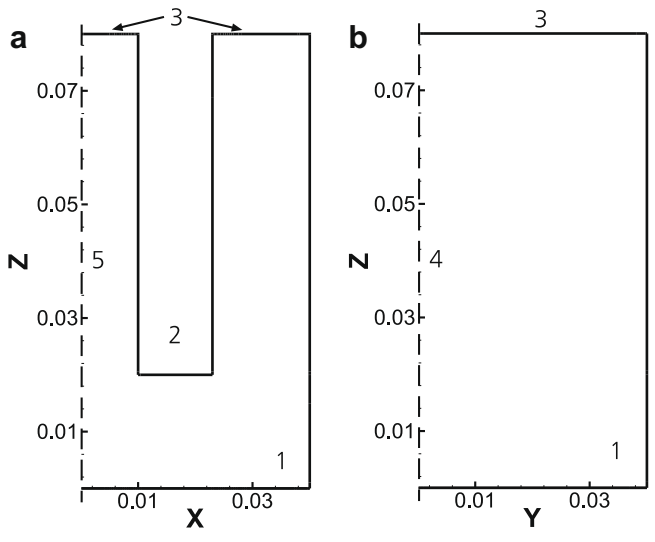

Fig. 2. Views of the symmetry planes of the glass bath at (a) $y = 0$ m and (b) $x = 0$ m with 1 being the crucible wall, 2 the electrode surface, 3 the free surface of the melt, 4 the symmetry plane $y = 0$ m and 5 the symmetry plane $x = 0$ m.

well studied. In this paper, we focus on the question, how thermal convection can be influenced by Lorentz forces $\mathbf{f_L}$. In practical applications one would like to know, how the homogeneity or mixing rate can be improved with such an additional force. To generate Lorentz forces we suppose that a homogenous and steady magnetic flux density $\mathbf{B}_0 = B_0\mathbf{e_y}$ is given for the whole crucible as indicated in Fig. 1. With the definition of $\mathbf{B}_0$ the imposed Lorentz force simplifies to

$$\mathbf{f_L} = f_{Lx}\mathbf{e_x} + f_{Lz}\mathbf{e_z} = J_z B_0 \mathbf{e_x} - J_x B_0 \mathbf{e_z}. \tag{3}$$

Hence, we have one Lorentz force component acting in $\mathbf{e_x}$-direction and one component acting in $\mathbf{e_z}$-direction, namely f_{Lx} and f_{Lz}. The model for constant U_E and B_0 holds also for a low frequency electric potential and a magnetic flux density of the same frequency which would be used in practice to minimize corrosion as at low frequencies the skin depth is large in comparison to the crucible dimensions.

In our considerations we neglect effects of induced currents and viscose heating which is usually valid for the flow of glass melts. To estimate these effects we take the following parameter values: $\sigma_0 \sim 1\text{–}10$ S/m, $\eta_0 \sim 1\text{–}10$ Pa s, $\lambda_0 \sim 1$ W/mK, $c_P \sim 1000$ J/kg K, $\rho_0 \sim 3000$ kg/m^3, a thermal expansion coefficient of $\beta \sim 10^{-4}$, a typical length scale of $L_0 \sim 0.04$ m, a typical velocity of $u_0 = 10^{-4}\text{–}10^{-2}$ m/s and a typical temperature difference of $\Delta T \sim 100$ K. For this scales the induced currents $\sigma(\mathbf{u_0} \times \mathbf{B_0})$ are negligible because of a small Hartmann number

$$\mathrm{Ha} = B_0 L_0 \sqrt{\frac{\sigma_0}{\eta_0}} \ll 1,$$

which describes the ratio between induced electromagnetic force and the friction force [8]. The viscose heating is negligible compared with the heat conduction since the ratio of both, the Brinkman number, is

$$\mathrm{Br} = \frac{\eta_0 u_0^2}{\lambda_0 \Delta T} \ll 1.$$

Furthermore, we do not take into account internal radiative heat transfer as the considered glass is almost completely non-transparent even for thin layers.

During our studies we only model the glass bath and assume laminar and steady flow. This assumption is valid due to the Rayleigh number Ra of the system, which is

$$\mathrm{Ra} = \frac{g\beta\Delta T L^3 \rho^2 c_P}{\eta_0 \lambda_0} < 10^5.$$

The change from a steady symmetric laminar (first instability) to a symmetry breaking but still steady and laminar regime (second instability) was observed for $\mathrm{Ra} > 10^5$ in convection cells with bottom-heated and top-cooled walls (Benard cells) [22,23] and in cavities with internal volumetric heat sources [24].

The three-dimensional steady flow is governed by the mass conservation equation

$$\nabla \cdot (\varrho \mathbf{u}) = 0, \tag{4}$$

and the Navier–Stokes equation

$$\nabla \cdot (\varrho \mathbf{u}\mathbf{u}) = -\nabla p + \nabla \cdot \left[\eta\left(\nabla \mathbf{u} + \nabla \mathbf{u}^T\right)\right] + \varrho g \mathbf{e_z} + (J_z \mathbf{e_x} - J_x \mathbf{e_z}) B_0, \tag{5}$$

with the following boundary conditions:

$$\mathbf{u} = 0 \quad \text{at the electrodes and crucible wall,} \tag{6}$$

$$\mathbf{u} \cdot \mathbf{n} = 0, \quad \nabla(\mathbf{u} \cdot \mathbf{t}) \cdot \mathbf{n} = 0 \quad \text{at the flat free surface,} \tag{7}$$

where $\mathbf{n}$ denotes the normal vector and $\mathbf{t}$ the tangential vector of the considered boundary faces. The left hand-side of the Navier–

Stokes equation (5) represents inertia whereas the right hand-side represents the body forces. The driving forces are the buoyancy and the imposed Lorentz force. The velocity boundary conditions are chosen to correspond to the physical model, i.e. no slip boundary condition at the crucible wall and the electrodes, Eq. (6), and free slip boundary condition at the flat free surface, Eq. (7).

The energy equation is solved to determine the temperature T of the melt. With the prescribed assumptions the equation for T is then

$$c_P \nabla \cdot (\mathbf{u} \varrho T) = \nabla \cdot (\lambda \nabla T) + \frac{J^2}{\sigma}, \tag{8}$$

with the boundary conditions

$$-(\lambda \nabla T) \cdot \mathbf{n} = h(T - T_\infty) \quad \text{at the crucible wall}, \tag{9}$$

$$-(\lambda \nabla T) \cdot \mathbf{n} = \epsilon \sigma_{sb}(T^4 - T_\infty^4) \quad \text{at the free surface}, \tag{10}$$

$$(\nabla T) \cdot \mathbf{n} = 0 \quad \text{at the electrodes} \tag{11}$$

with the ambient temperature T_∞, the emissivity ϵ and the Stefan–Boltzmann constant σ_{sb}. The energy equation (8) expresses the balance between heat convection on the left hand-side and heat conduction and heat production on the right hand-side. The heat transfer coefficient h specifies the convective heat transfer at all crucible walls, Eq. (9). Under the assumption that h is constant and equal for the whole crucible wall, we evaluated h theoretically. The derivation of h is given in Appendix A. At the free surface of the melt we assume radiative heat transfer expressed with the Stefan–Boltzmann law, Eq. (10), where ϵ has to be determined experimentally. The heat flux $(\nabla T) \cdot \mathbf{n}$ is assumed to be zero at the electrodes to be consistent with adiabatic conditions. Note, that effects of internal radiation are neglected throughout our considerations. To calculate the heat input q_{in} and the Lorentz force $\mathbf{f_L}$ we evaluate the Laplace equation for the scalar field of the electric potential ϕ, which is

$$\nabla \cdot (-\sigma \nabla \phi) = 0. \tag{12}$$

Eq. (12) results from Ampère's law $\nabla \cdot \mathbf{J} = 0$ and Ohm's law $\mathbf{J} = -\sigma \nabla \phi$. The electrodes and crucible wall are made of platinum with an electrical conductivity five orders of magnitudes higher than that of glass melt. Basically, we can assume that the electrodes and the crucible wall are equipotential surfaces with a constant electric potential, i.e. we define

$$\phi = \pm U_E/2 \text{ at the electrodes}, \tag{13}$$

$$\phi = 0 \text{ at the crucible wall}. \tag{14}$$

For the model the planes $x = 0$ m and $y = 0$ m are also the symmetry planes of the physical model. Firstly, the boundary conditions are applied symmetrically and secondly, the Rayleigh number does not exceed the critical Rayleigh number for symmetry breaking. We verified this assumption with simulations of the whole crucible for various parameter settings. Therefore, we only model a quarter of the glass melt in the crucible. We define the free slip boundary condition, Eq. (7), and the adiabatic boundary condition, Eq. (11), at both symmetry planes. If we have $\phi = -U_E/2$ at one electrode, $\phi = U_E/2$ at the other electrode, and $\phi = 0$ at the crucible wall, the symmetric electric field gives us

$$\phi = 0 \text{ at the plane } x = 0 \text{ m}, \tag{15}$$

$$(\nabla \phi) \cdot \mathbf{n} = 0 \text{ at the plane } y = 0 \text{ m}. \tag{16}$$

An analysis of the governing Eqs. (4)–(12) shows that the system is highly coupled. Beside the well known coupling of velocity and temperature field due to buoyancy in Eq. (5) and the heat convection in Eq. (8) we have a coupling with the Laplace equation (12) because of the Lorentz force and the Joule heat input in Eqs. (5) and (8), respectively. Overall, the strong variation of the physical properties of the glass melt leads to a strong coupling as well.

The main focus is to evaluate the governing Eqs. (4)–(12) and to obtain the unknowns of the system, which are the velocity $\mathbf{u}$ and temperature T. We like to obtain an understanding of the Lorentz force distribution and its effects on the flow. For this purpose we systematically vary the magnetic flux density B_0 and the electric potential difference U_E.

3. Implementation and numerical model

The calculations are performed for the composition 47.7%BaO–20.0%B_2O_3–27.1%SiO_2–5.2FeO_2 (all data in mass%), which is characterized by a low viscosity, e.g. $\eta = 1.2$ Pa s at a temperature of 1450 K. The composition results in a nearly black glass melt for which the internal heat transfer by radiation is negligible. The thermophysical properties have been measured and are given in Table 1. In Table 2 the remaining parameters are summarized.

The coupled set of Eqs. (4)–(12) has been solved using the commercial software FLUENT which is developed to calculate coupled thermohydrodynamic effects. Furthermore, it is possible to solve the transport equation for scalar fields, which we use to solve the Laplace equation (12). With User Defined Functions the Joule heat input and the Lorentz force are calculated and introduced to the Navier–Stokes equation (5) and the energy equation (8).

The descretization of the governing equations is done by the finite volume method [10]. For our calculations we have chosen the implicit method with second-order accuracy. The pressure and velocity are linked by the SIMPLE algorithm. We used the default setting for the under-relaxation factors except for the energy equation, which we set to 0.9 as the strong coupling may led to unintended oscillations if we had strong temperature variations. The calculations terminated if the residuals of the continuity and the velocity field were smaller than 10^{-6} and those of the energy and the scalar field were smaller than 10^{-9}. Furthermore, the convergence was tested for each set of parameters by comparing the volumetric heat input q_{in} with the heat loss over the crucible walls and the surface of the melt q_{out}. For $|q_{\text{in}} - q_{\text{out}}| < 10^{-3}$ we assumed convergence, which was the case for all presented results.

Fig. 3 shows views of the mesh, which was used for all presented calculations. The mesh consists of about 6.13×10^5 elements and is generated with GAMBIT. The surface of the melt is meshed using the boundary layer option for the crucible wall and the electrode. In the remaining area an unstructured face mesh is created which consists of quadrilateral mesh elements. The mesh node pattern of this source-face is projected through the volume with the Cooper meshing algorithm [11].

The number of cells (a) in the whole volume, (b) close to the free surface, (c) around the electrode and (d) at the crucible wall may significantly influence the results. The goal of the following mesh analysis is to find a mesh which maps all parameters of the system and the material properties very well. The influence of the mesh

Table 1
Thermophysical properties of the composition 47.7%BaO–20.0%B_2O_3–27.1%SiO_2–5.2FeO_2 (all data in mass%).

Property	Glass 3
Viscosity η	9.92×10^{-2} Pa s $\cdot \exp\left(\frac{1046.20\ \text{K}}{T - 1033.41\ \text{K}}\right)$
Electrical conductivity σ	$1.74 \times 10^6 \frac{S}{m} \cdot \exp\left(-\frac{20.300\ \text{K}}{T}\right)$
Density ρ	$3931.5 \frac{\text{kg}}{\text{m}^3} - 0.3953 \frac{\text{kg}}{\text{m}^3\,\text{K}} \cdot T$
Heat conductivity λ	$2 \times 10^{-6} \frac{\text{W}}{\text{mK}^3} \cdot T^2 - 3.2 \times 10^{-3} \frac{\text{W}}{\text{mK}^2} \cdot T + 2.68 \frac{\text{W}}{\text{mK}}$
Heat capacity c_P	$1285 \frac{J}{\text{kg K}}$

Table 2
Parameter settings.

Parameter	Value
Heat transfer coefficient h	$4\,\frac{W}{m^2\,K}$
Emissivity ϵ	0.6
Ambient temperature T_∞	1393 K
Stefan–Boltzmann constant σ_{sb}	$5.67\times10^{-8}\,\frac{W}{m^2\,K^4}$

resolution is studied separable for (a)–(d) with the test case $U_E = 15$ V and $B_0 = -40$ mT. The meshes were validated on the basis of the maximum temperature T_{max} in the melt. In Fig. 4 the evolution of T_{max} for each region of refinement (a)–(d) is shown.

Lets discuss in detail the need of refinement for the cases (a)–(d):

(a) During the first mesh study we changed the average size of all grid elements by varying the hight of the cells outside the boundary layers from 1×10^{-3} m to 7.5×10^{-4} m and 5×10^{-4} m and keeping all other settings of the mesh constant. In Fig. 4(a) a change of T_{max} can be observed tending to an asymptotic value for decreasing element size. As the reduction of the element size leads to an explosive increase of the overall cell number and therefore to an explosive increase of the computational time we have chosen an average element size of 7.5×10^{-4} m for he final mesh.

(b) As we expected large temperature gradients at the surface of the melt, we compared meshes with boundary layers thicknesses ranging from 8×10^{-3} m to 1×10^{-2} m and a thickness of the smallest cells ranging from 1×10^{-3} m to 4×10^{-4} m, 2×10^{-4} m and 1×10^{-4} m. For this mesh studies we observed the maximum variations in T_{max} as shown in Fig. 4(b). But again the rate of changes also reduces with reducing element size and tends to an asymptotic value. As the ratio width/hight of an element should not exceed 1/10 [10], and the average width of a surface element is 1×10^{-3} m we have chosen an element thickness of 1×10^{-4} m.

(c) The need to study the influence of the grid size around the electrode is twofold. First, the electric current flowing from one rod electrode to another meets the greatest electric current density in the immediate vicinity of the electrodes. Consequently, these regions acquire high local temperatures. As the electrical conductivity is increasing exponentially with the temperature, a good mapping of the property law $\sigma(T)$ requires a fine mesh in hot regions of the melt. Furthermore, at the squared edges of the electrode the exact solution of the Laplace equation (12) has a singularity. The numerics yields in high values of $\nabla\phi$ at the edges which require a refinement as well [19]. We have compared a mesh without boundary layer around the electrode with two meshes with a boundary layer thickness of $\delta = 5\times10^{-3}$ m and the smallest cell sizes of 4×10^{-4} m and 2×10^{-4} m. A significant change can be observed if we compare meshes without boundary layer. A refinement of the boundary layer cells leads to an rapid convergence towards an asymptotic value, see Fig. 4(c).

(d) The Prandtl number Pr, which describes the ratio between thermal and viscous diffusion, is for glass melts about $Pr \approx 100$. Furthermore, it is a measure of the ratio between the velocity boundary layer thickness δ_s and the temperature boundary layer thickness δ_t. As the relation $Pr^{1/2} \sim (\delta_s/\delta_t)$ is valid for laminar flow at a flat plate [36], we can expect that δ_t is about 10 times smaller than δ_s. Due to the small dimensions we do not expect free flow and have the smallest velocity boundary layer thickness between the electrode and the crucible wall with $\delta_s = 8.5\times10^{-3}$ m, and hence at theoretical thermal boundary layer thickness of $\delta_t = 8.5\times10^{-4}$ m. A proper resolution with 10 cells requires an average cell thickness of 8.5×10^{-5} m. We studied the influence of the resolution of the thermal boundary layer by refining the thickness the smallest cells at the crucible wall from 4×10^{-4}, 2×10^{-4}, 1×10^{-4} to 5×10^{-5}. The results in Fig. 4(d) show that the influence of the boundary layer thickness at the crucible wall is negligible.

4. Selected results

During our simulations we vary the magnetic flux density between $-120\,\text{mT} \leqslant B_0 \leqslant 120\,\text{mT}$ and the electric potential difference between $3\,\text{V} \leqslant U_E \leqslant 18\,\text{V}$. This is the order of magnitude of effective magnetic flux densities one can generate for low frequencies as it is used in the laboratory experiment [20]. For the chosen parameter range of U_E we are in a thermally stable regime and can perform steady calculations. For larger U_E the increasing temperature leads to an exponential increase of $\sigma(T)$ and thus, an amplification of q_{in}. The heat transport mechanism in the melt are not able to compensate q_{in} which results in higher temperatures. This self-induced runaway of the temperature is also denoted as *thermal*

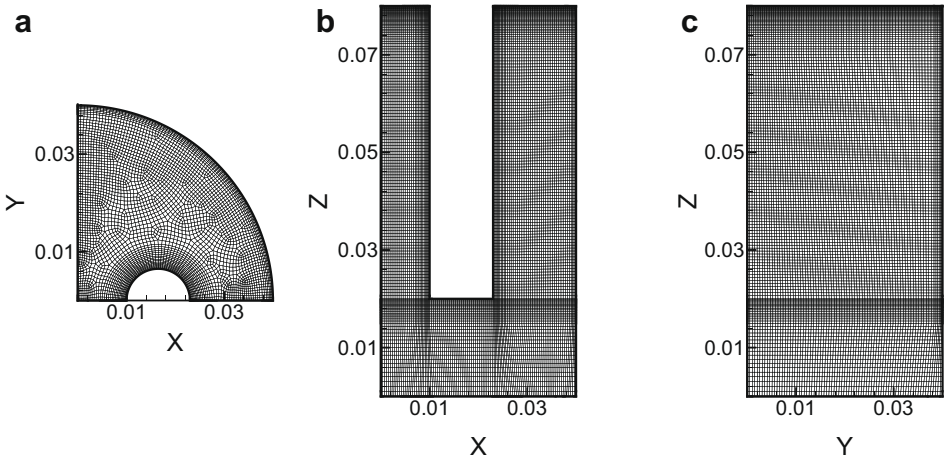

Fig. 3. Mesh for the quarter crucible corresponding to Fig. 1 at (a) $z = 0.04$ m, (b) the symmetry plane $y = 0$ m and (c) the symmetry plane $x = 0$ m.

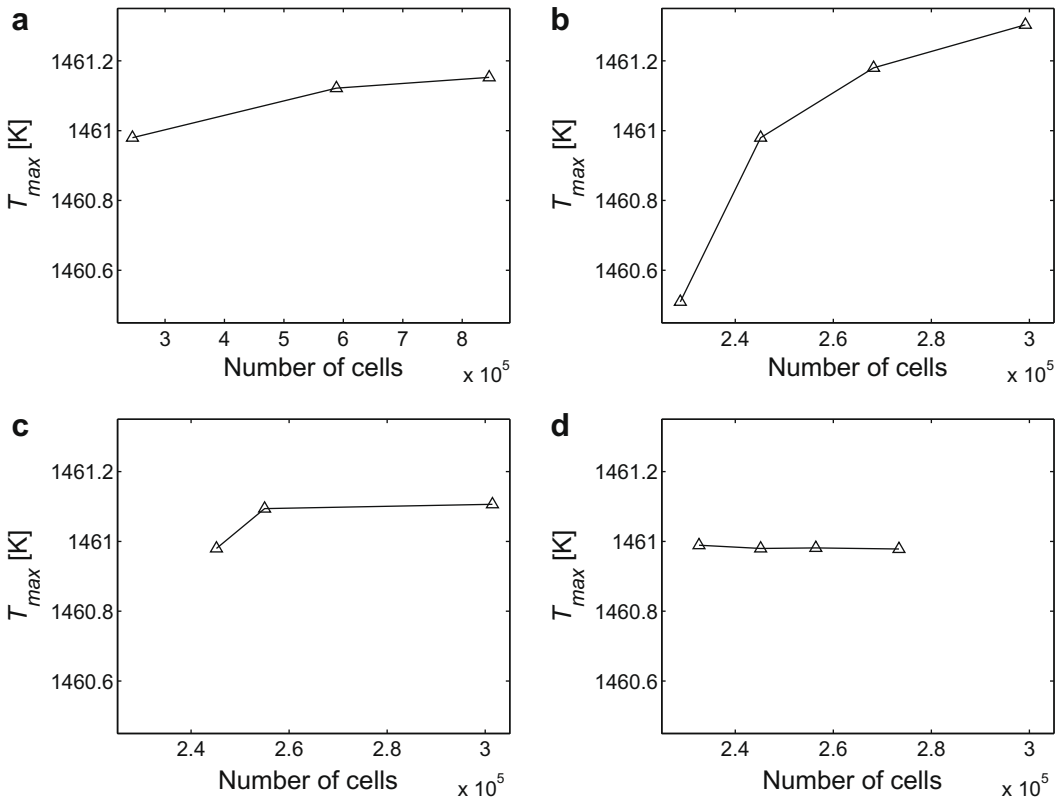

Fig. 4. Studies of the mesh on the basis of the maximum temperature in the melt T_{max} for varying element size: (a) size of the elements in the whole volume, (b) the element height below the free surface, (c) grid size of the elements around the electrode and (d) at the crucible wall.

instability [32,35] and can only be avoided by controlling the heat input q_{in} over the electrode potential [34] which requires time-dependent calculations. The experiments [20] are conducted in a thermally unstable regime. The heat input q_{in} is kept constant by continuous regulation of U_E between 21 V and 22 V. Therefore, a direct comparison of the results is not possible. The numerical simulations presented in [2] reach the temperature range of the experiment with $U_E > 18$ V and steady calculations. On the first sight this seems to be a contradiction to the statement about thermal instability just given. But the physical model of the numerics in [2] contains a rough simplification as the authors define a constant temperature at the crucible wall. This boundary condition imposes a certain temperature range and avoids thermal instability. But the presented flow pattern looks like the flow in so-called Hedly cells, as the fluid is flowing downwards at all parts of crucible wall. In our opinion the chosen boundary condition is not correct. In reality the temperature at the wall is not controlled to a defined value. Instead, the heat transport at the wall is dominated by convection at the outer surface. Therefore, the direct comparison of the simulation and the experiment as given in [2] is not possible and does not contribute to a better understanding of the physical phenomena in electromagnetically controlled convection of glass melt.

Before we discuss the influence of the Lorentz force on the velocity and temperature field let us have a closer look at the Lorentz force distribution itself.

4.1. Lorentz force distribution

Both components of the Lorentz force, $f_{Lx} = \mathbf{f_L} \cdot \mathbf{e_x}$ and $f_{Lz} = \mathbf{f_L} \cdot \mathbf{e_z}$, see Eq. (3), can be rewritten in terms of the electric potential ϕ and become

$$f_{Lx} = -\sigma(T) B_0 \frac{\partial \phi}{\partial z} \text{ and } f_{Lz} = \sigma(T) B_0 \frac{\partial \phi}{\partial x}.$$

The sign, and hence the orientation of f_{Lx} and f_{Lz}, can basically be defined by the constant magnitude of the magnetic flux density B_0 and the gradient of the electric potential $\nabla\phi$. As the orientation of $\nabla\phi$ is fixed with the boundary condition at the electrodes, Eq. (13), we reverse the direction of f_{Lx} and f_{Lz} with the sign of B_0.

The spatial distribution of the Lorentz force is specified by the temperature-dependent electrical conductivity $\sigma(T)$ and the gradient of the electric potential $\nabla\phi$. An example for the isolines of ϕ is shown in Fig. 5 for the planes $y = 0$ m and $z = 0.04$ m. On the level of the electrodes with $z \geqslant 0.02$ m we mainly find components of $\partial\phi/\partial x$, see Fig. 5(a). The dashed lines in the view of plane $z = 0.04$ m in Fig. 5(b) further show that $\partial\phi/\partial x$ is zero at around $|x| \approx 0.0165$ m. Thus, at the height of the electrodes we only have components of f_{Lz} with reversing orientation at almost straight lines with $|x| \approx 0.0165$ m. High values of $\partial\phi/\partial x$ – hence of f_{Lz} – can be expected around the electrodes due to very close isolines of ϕ. As ϕ hardly changes at $|y| \geqslant 0.025$ m we expect very small magnitudes of f_{Lz} in this region of the crucible. Also below the electrodes the influence of $\partial\phi/\partial x$ weakens. Here, the intensity of $\partial\phi/\partial z$ is high, whereas $\partial\phi/\partial z$ is negligible in all other parts of the crucible. Therefore, the Lorentz force component f_{Lx} can only be observed below the electrodes.

As the electrical conductivity σ is a function of the temperature, the temperature distribution has also an impact on the magnitude of the Lorentz force. In hot regions the increasing values of $\sigma(T)$ lead to an amplification of the Lorentz force. In general the hot regions – also called *hot spots* – are located around the electrodes with already large $\nabla\phi$. Depending on the flow direction we observe hot fluid between the electrodes and at the bottom of the electrodes. The left diagrams in Fig. 6 give the vector field of $\mathbf{f_L}$ in the symmetry planes $x = 0$ m and $y = 0$ m for $B_0 = 80$ mT (first row) and $B_0 = -80$ mT (second row). We like to emphasize that the impact of both components f_{Lx} and f_{Lz} is supportive and does

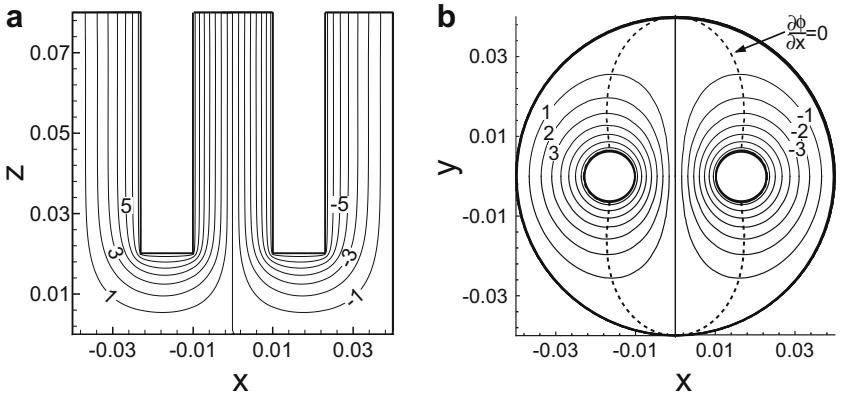

Fig. 5. Distribution of the electric potential ϕ in V for $U_E = 15$ V in the plane (a) $y = 0$ m and (b) $z = 0.04$ m.

not conflict. We observe large values of f_L at the squared edges of the electrodes. The numerics leads to large values of $\nabla\phi$ as the exact solution of the Laplace equation (12) has a singularity at squared edges [19]. As the high values are restricted to a tiny region, their influence on the result is small. The view of the plane $z = 0.04$ m in the right diagrams of Fig. 6 shows f_{Lz}. As expected we find the largest values in the vicinity of the electrodes along $y = 0$ m and a reversing orientation at around $|x| \approx 0.0165$ m. The isolines of $B_0 = 80$ mT (first row) and $B_0 = -80$ mT (second row) have slightly different paths as result of the unequally distributed temperature-dependent electrical conductivity.

4.2. Velocity and temperature distribution

Before we discuss the influence of the imposed Lorentz force let us shortly look at the velocity and temperature field of the pure thermal convection with $B_0 = 0$ T and $U_E = 15$ V which are shown in the first row of Fig. 7. In the left and right diagrams of Fig. 7 the vector field of the velocity $\mathbf{u}$ and the temperature T are given for both symmetry planes, namely the plane $y = 0$ m, ranging from $0\text{ m} \leqslant x \leqslant 0.04$ m, and the plane $x = 0$ m, ranging from $0\text{ m} \leqslant y \leqslant 0.04$ m. The diagrams in the middle of Fig. 7 show the z-component of the velocity $u_z = \mathbf{u} \cdot \mathbf{e_z}$ in the plane $z = 0.04$ m. The positive values of u_z indicate that the upward streams are located around the electrodes for pure thermal convection. We have the largest velocities in the center of the crucible with $x = y = 0$ m. The fluid flows downward in the remaining parts at the crucible wall with approximately $|y| \geqslant 0.018$ m (indicated by the dashed lines). In the left diagram of Fig. 7 one can clearly see that the pure thermal convection mainly involves the fluid at the level of the electrodes. Below the electrodes there is no driving buoyancy force due to the well stratified temperature layers with hot fluid close to the electrode and cold fluid close to the crucible bottom. Consequently, the melt hardly flows in this region and therefore is badly stirred. In the vicinity of the electrodes the fluid is heated up while it is flowing upwards and we find the highest temperatures just be-

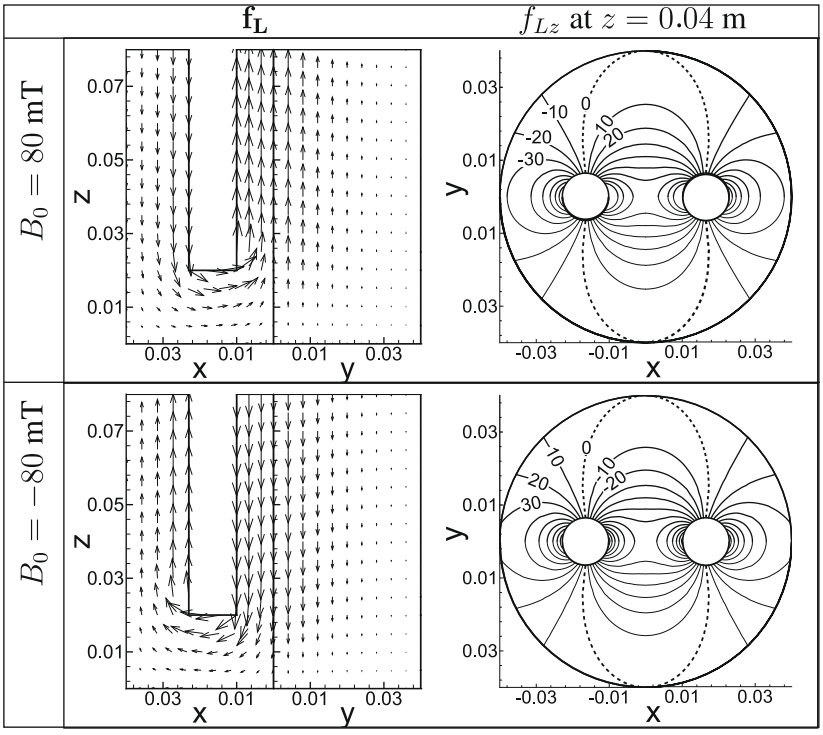

Fig. 6. Lorentz force distribution for $B_0 = 80$ mT (first row) and $B_0 = -80$ mT (second row) and $U_E = 15$ V. The left diagrams give the vector field of $\mathbf{f_L}$ at the planes $y = 0$ m and $x = 0$ m. The right diagrams give the isolines of the z-component of the Lorentz force f_{Lz} at $z = 0.04$ m.

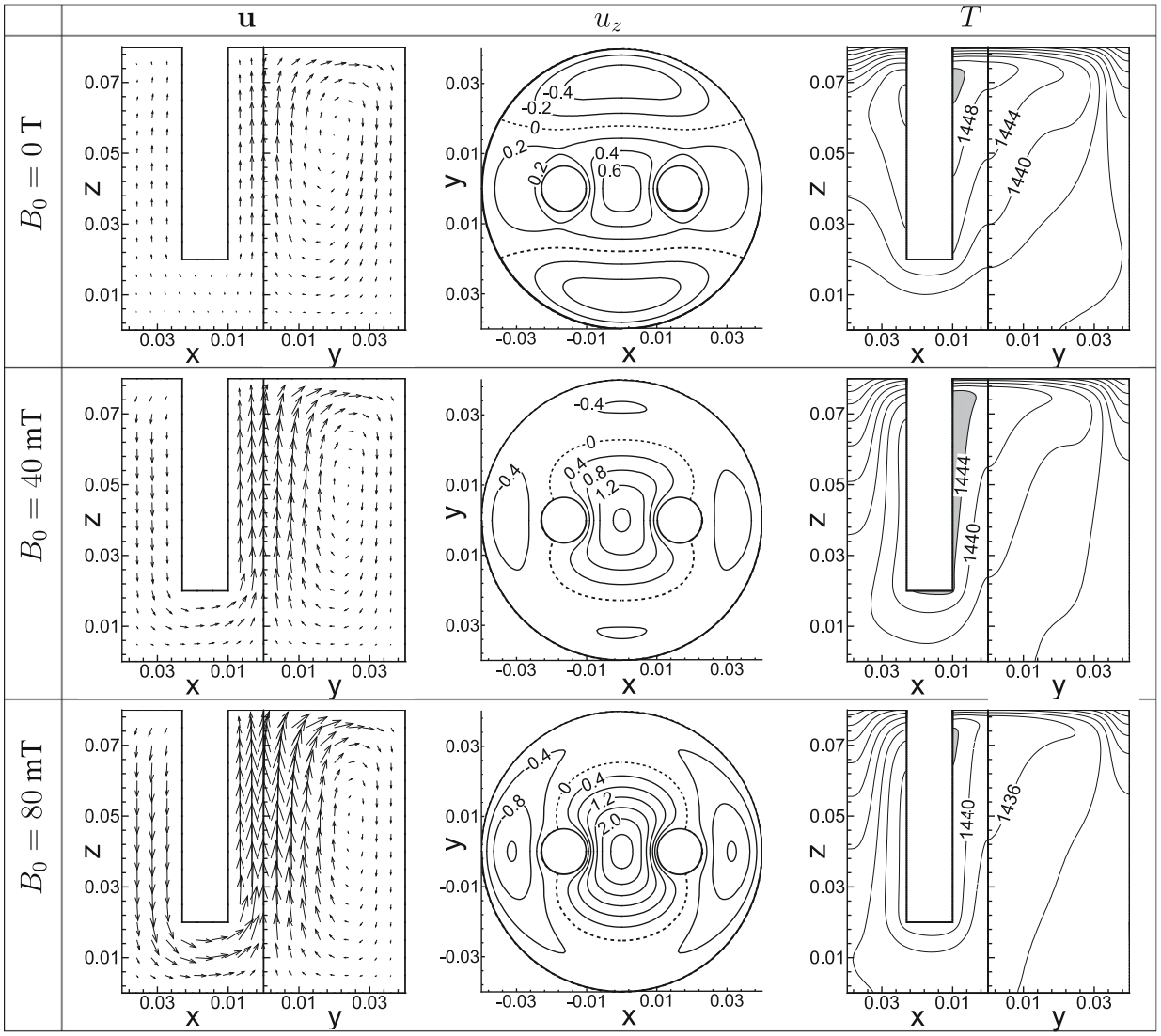

Fig. 7. The vector field of the velocity **u** (left), isolines of the *z*-component $u_z = \mathbf{u} \cdot \mathbf{e_z}$ in mm/s (middle) and the temperature T in K (right) for $B_0 = 0$ T, $B_0 = 40$ mT, $B_0 = 80$ mT (starting from the first row) and $U_E = 15$ V. The velocity field **u** and the temperature T are shown for both symmetry planes, namely the plane $y = 0$ m and the plane $x = 0$ m. The *z*-component of the velocity u_z is plotted in the plane $z = 0.04$ m. The regions with the largest temperature, so called hot-spots, are highlighted in grey.

low the surface of the melt. The fluid cools down at the surface and the crucible wall. As the heat loss by radiation at the surface is larger than the convective heat transfer at the crucible wall we obtain large temperature gradients at the free surface as expected.

Starting from a system with pure thermal convection we increase stepwise B_0 with $B_0 > 0$ T and $U_E = 15$ V. In the second and third row of Fig. 7 diagrams for $B_0 = 40$ mT and $B_0 = 80$ mT are given. The vector plots (left) and the contour plot of u_z (middle) show that the vertical component of the Lorentz force f_{Lz} in the center increases **u** significantly. The downward Lorentz force between the crucible wall and the electrode leads to a change of the flow direction in this part of the crucible already for $B_0 =$ 20 mT (not shown here). But not only the velocity at the level of the electrodes is affected. The horizontal component of the Lorentz force f_{Lx} controls the fluid flow below the electrodes. The significant increase of **u** in this region is illustrated in Fig. 8(a). It gives the velocity magnitude $u = |\mathbf{u}|$ measured in terms of velocity magnitude without Lorentz force $u_0 = u(B_0 = 0\,\text{T})$ along the centerline of the crucible ($x = y = 0$ m). Already at the level of the electrodes u increases by a factor of two for $B_0 = 40$ mT and by a factor of approximately 3.5 for $B_0 = 120$ mT. But close to the bottom u multiplies by almost a factor of four ($B_0 = 40$ mT) up to eight ($B_0 =$ 120 mT), thanks to f_{Lx}. The Lorentz force does not only increase the overall velocity, it captures also a region which is not affected by the buoyancy force and therefore leads to a strong improvement of the stirring. We can state that the Lorentz force distribution $\mathbf{f_L}$ is mainly taken over by the velocity field **u**. Consequently, the magnitude of the downward stream in the *yz*-plane reduces with increasing B_0. Furthermore, the fluid at the bottom of the crucible with $y \geqslant 0.025$ m is still almost immobilized as the Lorentz force is very weak. The increase of u with B_0 results in a better temperature homogenization as the values of the highest temperature decrease. Fig. 8(b) illustrates the temperature homogenization on the basis of the temperature along $x = y = 0$ m.

Now we reverse the direction of the magnetic field and decrease the magnetic field stepwise starting again from $B_0 = 0$ T. First let us consider cases with $B_0 = -40$ mT and $B_0 = -70$ mT which are shown in the second and third row in Fig. 9. Now the vertical component of the Lorentz force f_{Lz} supports the thermally driven upward flow between the crucible wall and the electrodes as u_z increases, compare u_z for $B_0 = 0$ T with u_z for $B_0 = -40$ mT and $B_0 = -70$ mT in Fig. 9. Again, f_{Lx} controls the flow below the electrodes. In contrast to the cases with $B_0 > 0$ T, the fluid flows from the center to the crucible wall below the electrode. Between the

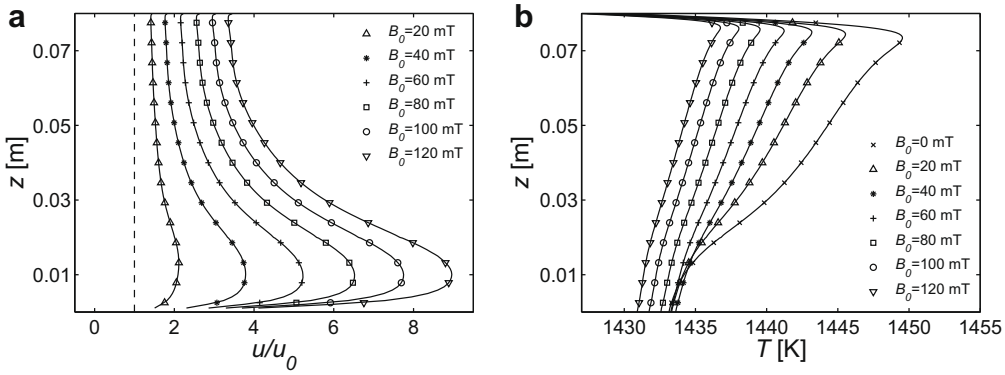

Fig. 8. (a) The velocity ratio u/u_0 gives the proportion of the velocity magnitude $u = |\mathbf{u}|$ with Lorentz force for $B_0 > 0$ T in comparison to that without Lorentz force $u_0 = u(B_0 = 0\,\text{T})$ in the centerline of the crucible ($x = y = 0$ m) and $U_E = 15$ V corresponding to Fig. 7. The dashed line gives $u = u_0$. In (b) the corresponding temperature distribution is shown.

electrodes the downward acting Lorentz force does not lead to an abrupt overall change of the flow direction. At the upper half level of the electrodes u_z is still positive, but the magnitude is reduced significantly compared to the thermally driven flow with $B_0 = 0$ T (first row in Fig. 10). The upward stream is driven by buoyancy due to the large temperature gradients just below the surface. Just the fluid below approximately $z = 0.03$ m ($B_0 = -70$ mT) is flowing downwards with a very small magnitude driven by Lorentz force. However, the small magnitudes of the velocity are an indicator for almost equally forces – neither buoyancy nor Lorentz force is clearly dominating in the center of the crucible. As a result, the region of the almost stagnant flow regime at the bottom of the center expands. On the one hand, $\mathbf{f_L}$ leads to a better motion below the electrodes and larger velocities at the crucible wall. On the other hand, the motion between the electrodes slows down and leads to an extension of the almost stagnant flow at the crucible bottom. At the same time the magnitude of the downward stream at the crucible wall and its proportion in the plane $x = 0$ m, both increase. Fig. 10(a) shows the reduction of u in the centerline for $B_0 = -20$ mT, -40 mT and -60 mT in comparison to $u_0 = u(B_0 = 0\,\text{T})$. Especially for $z \leqslant 0.03$ m u reduces dramatically and reaches nearly zero. Due to the low velocities in the centerline the temperatures between the electrodes and the temperature differences increase significantly as it is shown in Fig. 10(b).

If we now slightly change the magnetic flux density from $B_0 = -70$ mT to $B_0 = -71$ mT we observe a drastic change in the flow pattern and temperature distribution, compare third and forth row of Fig. 9. In the centerline buoyancy cannot compensate f_{Lz} which leads to a change of flow direction with large changes of the velocity magnitude. Now the fluid in the vicinity of the centerline is flowing downwards, moving below the electrodes to the crucible wall and between the crucible wall and the electrode to the surface. The velocity magnitude in the center, especially for $z < 0.03$ m, is now again a multiple of that without Lorentz forces, see curves with $B_0 = -80$ mT, -100 mT, -120 mT in Fig. 10(a). For $B_0 \leqslant -71$ mT the qualitative picture of the velocity field $\mathbf{u}$ corresponds to the distribution of the Lorentz force $\mathbf{f_L}$ and hence, is now opposite to that of $B_0 > 0$ T. Still we find the largest temperature in the vicinity of the electrodes, but now at their bottom as the fluid is heated up while it is flowing downwards between the electrodes.

If we now start at a converged solution with $B_0 \leqslant -71$ mT and increase stepwise B_0 the transition of the flow pattern takes place at different B_0. We pass through a hysteresis for which we obtain two different steady solutions with unequal flow pattern for one set of parameters depending on the starting condition of the calculations. The cases with a dominating upward stream between the electrodes we name 'upper branch' of the hysteresis and the cases with dominating downward stream we name 'lower branch'. Let us stress that the transition from the upper to the lower branch is characterized by an abrupt change of the flow pattern. For all U_E we studied this transition of the flow happens in the same manner like the already described one for $U_E = 15$ V. In contrast there exist qualitative differences for the transition from the lower to the upper branch of the hysteresis depending on U_E. If we assume a minimum change of the magnetic flux density of 1 mT, the transition is more like a jump for $U_E = 9$ V and $U_E = 12$ V. For $U_E = 15$ V and $U_E = 18$ V we observe a more continuous change of the flow pattern. Let us first look at the transition from the lower to the upper branch for $U_E = 15$ V given in Fig. 11. Here, converged solutions of the lower branch are used as starting condition for a system with increasing B_0. The first row of Fig. 11 gives the solution for $B_0 = -70$ mT which we obtained using the converged solution for $B_0 = -71$ mT (last row in Fig. 10) as starting condition. The differences between the flow pattern and temperature distributions of the solutions of the upper branch (third row of Fig. 10 with $B_0 = -70$ mT) and the lower branch (first row of Fig. 11 with $B_0 = -70$ mT) are obvious. Like in the case with $B_0 = -71$ mT we find a downward stream between the electrodes, upward streams between the crucible wall and one electrode and the hot spot just below the bottom of the electrodes for $B_0 = -70$ mT on the lower branch. If we reduce the Lorentz force by increasing B_0 to -50 mT (second row in Fig. 11) the motion decelerates in general and buoyancy becomes more relevant in some regions of the melt. As shown in the plane $x = 0$ m the temperature gradients just below the surface lead to an enormous deceleration of the downward motion. The same holds for the region between the electrodes with approximately $z \leqslant 0.04$ m. A further reduction of the Lorentz force results in a change of the flow direction in these regions. The flow splits into several vortices which can be seen in the plane $x = 0$ m for $B_0 = -45$ mT (third row of Fig. 11). For $z < 0.035$ m the fluid flows up with the lower vortex having a very small magnitude. For $z > 0.035$ m the motion is still dominated by Lorentz force and flows downwards. The isolines of u_z show that the downward flow between the electrodes is limited to a small region (bounded by the dashed lines). When increasing B_0 per 5 mT to $B_0 = -40$ mT the Lorentz force driven downward flow between the electrodes is limited to $z \geqslant 0.05$ m. But in the centerline the velocity magnitude of the downward flow is still larger than the magnitude of the upward flow. While we increase B_0 from -70 mT up to -40 mT the hot spot in the vicinity of the electrodes moves from the bottom of the electrodes ($B_0 = -70$ mT) to the region between the electrodes. There, the hot spot is moving from $z \approx 0.023$ m ($B_0 = -50$ mT) to $z \approx 0.048$ m ($B_0 = -40$ mT). The downward stream

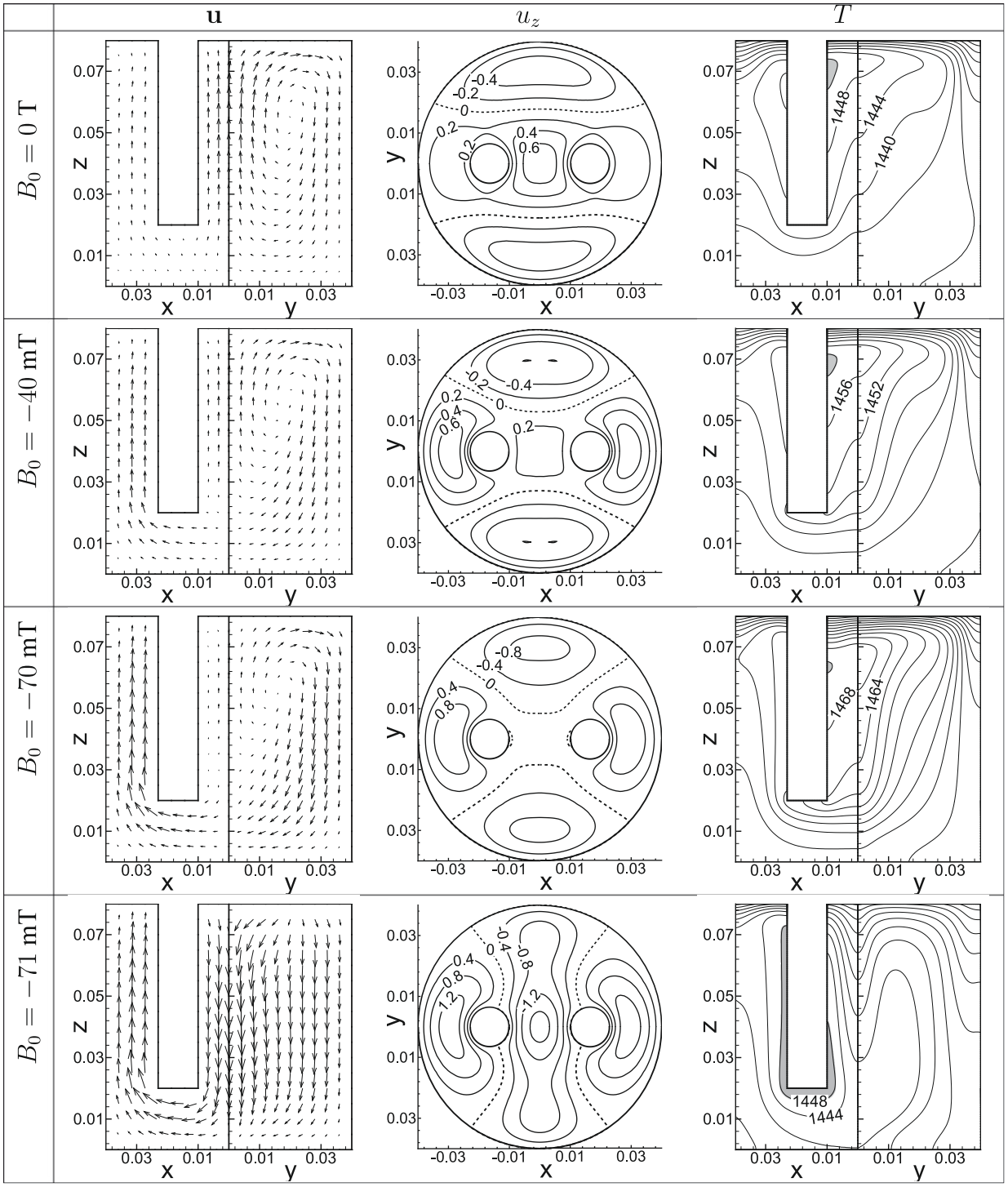

Fig. 9. The vector field of the velocity **u** (left), isolines of the z-component $u_z = \mathbf{u} \cdot \mathbf{e_z}$ in mm/s (middle) and the temperature T in K (right) for $B_0 = 0$ T, $B_0 = -40$ mT, $B_0 = -70$ mT, $B_0 = -71$ mT (starting from the first row) and $U_E = 15$ V. The results are obtained by starting from a system with $B_0 = 0$ T and reducing stepwise B_0. Always a converged solution is used as starting condition for the calculation with reduced B_0.

between the electrodes disappears completely for $B_0 = -39$ mT as shown in the last row of Fig. 11. Thus, the transition from the lower to the upper branch is characterized by the merging of the two vortices in the centerline to a single vortex.

Fig. 12 illustrates the transition from the lower to the upper branch for $U_E = 12$ V. Just before the transition, $B_0 = -46$ mT, buoyancy leads to a reversing of the flow direction only in the centerline with $z \leqslant 0.032$ m. The temperature gradient below the surface does not lead to upward streams and hence, the flow does not split into several vortices.

One possibility to illustrate the regime of the two-valued solutions and the transition of the flow pattern is to look at the maximum z-component of the velocity at $x = y = 0$ m, which we label as u_{zmax}. The transition of the flow pattern is characterized by a shift of the sign of u_{zmax}, whereas u_{zmax} is greater than zero at the upper branch and smaller than zero at the lower branch.

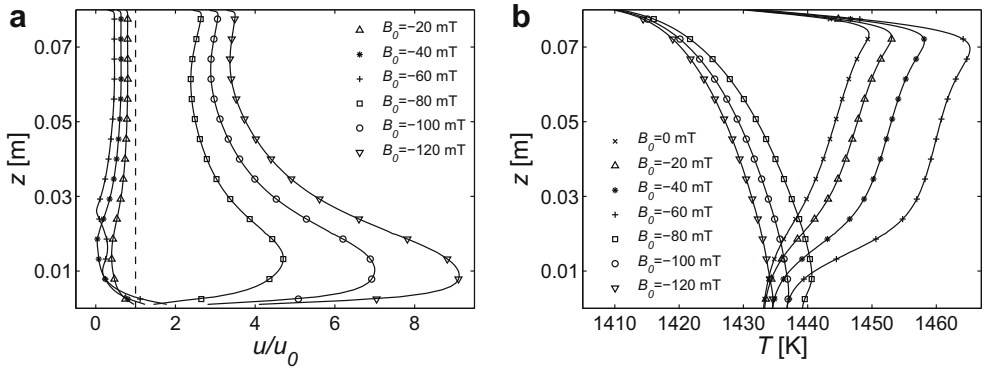

Fig. 10. Profile for upward Lorentz force in the center of the crucible of (a) the velocity ratio u/u_0 and (b) the temperature distribution T for $U_E = 15$ V. For $u/u_0 < 1$ the velocity with Lorentz force u is smaller than that without Lorentz force u_0.

In Fig. 13(a) u_{zmax} is given as a function of B_0 for various U_E. The right diagram gives a detailed view of the region with two solutions. First of all, the region of two-valued solutions $u_{zmax}(B_0)$ depends on U_E. As summarized in Table 3 we obtain two solutions between $-58\text{ mT} \leqslant B_0 \leqslant -46\text{ mT}$ for $U_E = 9$ V. This range expands to $-71\text{ mT} \leqslant B_0 \leqslant -46\text{ mT}$ if we consider $U_E = 12$ V. A further increase of the electric potential difference to $U_E = 15$ V only leads to a similar parameter range of two solutions, which is $-70\text{ mT} \leqslant B_0 \leqslant -40\text{ mT}$. For $U_E = 18$ V the change from $u_{zmax} > 0$ to $u_{zmax} < 0$ happens if we start at a steady solution with $B_0 = -56$ mT and apply $B_0 = -57$ mT. Therefore, the parameter range with two steady solutions changes to $-56\text{ mT} \leqslant B_0 \leqslant -27\text{ mT}$. In Fig. 13(b) u_{zmax} is measured in terms of the maximum z-component of the velocity without Lorentz force, $u_{zmax,0} = u_{zmax}(B_0 = 0)$. The diagram $u_{zmax}/u_{zmax,0}(B_0)$ confirms that the velocity linearly increases with B_0 for $B_0 > 0$ T. The deceleration of the motion in the upper branch with $B_0 < 0$ T is reflected in Fig. 13(b) as $0 < u_{zmax}/u_{zmax,0} < 1$.

4.3. Maximum stretching function

For the application not only the effects of the Lorentz force on the temperature distribution and velocity field are important. Especially the effect on the homogenization – how the mixing in laminar flow can be improved – is of interest. Laminar mixing is characterized by molecular diffusion on the interfaces between two fluids or inhomogeneities. It is based on interfaces increase by deformation of fluid volumes. There exist different definitions to quantify the mixing effect [31]. Typically deformations of infinitesimal elements, lines, surfaces and volumes are used which are based on the stretching function. The stretching function is a measure of the deformation velocity of an element and its theoretical maximum value α is given by [33]

$$\alpha = \sqrt{\mathbf{D} : \mathbf{D}}, \tag{17}$$

where $\mathbf{D} = 1/2(\nabla\mathbf{u} + (\nabla\mathbf{u})^T)$ is the symmetric stretching tensor. As pure rotation does not contribute to the deformation of fluid volumes the antisymmetric vorticity tensor is not part of the definition of α. α can easily be obtained from presented simulation data of the velocity field. Large α lead to large deformations and an increase of the interface between the fluid volumes. The goal of each mixing techniques is to maximize the deformation and hence, to maximize α in the whole volume. It is a first step towards the evaluation of the influence of the Lorentz force on laminar mixing.

Fig. 14 shows isolines of α for pure thermal convection (first row) and for Lorentz force dominated flows with $B_0 = 80$ mT (second row) and $B_0 = -80$ mT (third row). Due to low velocities below the electrodes and close to the bottom for $B_0 = 0$ T, α is very small in this region as indicated by the grey shaded areas. Larger α we find around the electrodes and for $y \geqslant 0.035$ m in the plane $x = 0$ m because of the additional isolines. In Lorentz force dominated regimes (second and third row of Fig. 14) α increases significantly as the grey shaded areas almost disappeared, especially close to the bottom for $z \leqslant 0.02$ m. We can observe some differences in the α distribution for $B_0 = 80$ mT and $B_0 = -80$ mT even though the magnitude of both magnetic flux densities is equal and the flow is dominated by the Lorentz force. For $B_0 = 80$ mT α hardly changes for $y \geqslant 0.025$ m. But for $B_0 = -80$ mT we observe a slight increase of α in this region due to closer isolines. The largest values of α we find in the vicinity of the electrodes for both signs of B_0. In the case of $B_0 = 80$ mT the isoline density is largest between the electrodes. In contrast the isoline density ist largest between the crucible wall and one electrode for $B_0 = -80$ mT.

Slight differences also exist between the solutions of the upper and the lower branch of the two-valued regime which are obtained with the same set of parameters. As shown in Fig. 15 for $B_0 = -40$ mTα differs in the region between the electrodes. Due to the split of the flow in vortices α is larger for the solutions of the lower branch (second row in Fig. 15) than for the upper branch (first row in Fig. 15) of the hysteresis.

4.4. Global analysis

During the discussions in the previous section we gained a good insight into the electromagnetically flow control by studying flow pattern, temperature distributions, variations of local velocities and temperatures and the distribution of the maximum stretching function. In this section a coarse measure of the overall influence of the imposed Lorentz force on the flow can be given with volume averaged quantities.

First of all we define the volume averaged velocity magnitude $\bar{u}$ according to

$$\bar{u} = \sqrt{\int_{(V)} |\mathbf{u}|^2 \, dV / V}. \tag{18}$$

In Fig. 16 $\bar{u}$ is given in terms of $\bar{u}_0 = \bar{u}(B_0 = 0\text{ T})$. Note that $\bar{u}/\bar{u}_0$ is never smaller than unity except for $B_0 = -20$ mT and $U_E = 15$ V. It indicates that the Lorentz force leads to an overall increase of the kinetic energy for almost all considered cases. For $B_0 \geqslant 20$ mT $\bar{u}$ is almost a linear function of B_0 and can become a multiple of $\bar{u}_0$, e.g. $\bar{u} \approx 2\bar{u}_0$ for $U_E = 15$ V, $B_0 = 60$ mT and $\bar{u} \approx 3\bar{u}_0$ for $U_E = 15$ V, $B_0 = 100$ mT. In general, the larger U_E and B_0 become, the larger is the ratio $\bar{u}/\bar{u}_0$. For $B_0 < 0$ T the discontinuous transition of the flow pattern from $u_{zmax} > 0$ to $u_{zmax} < 0$ is reflected by a jump in the graph $\bar{u}/\bar{u}_0(B_0)$. Again, after the change of the flow direction

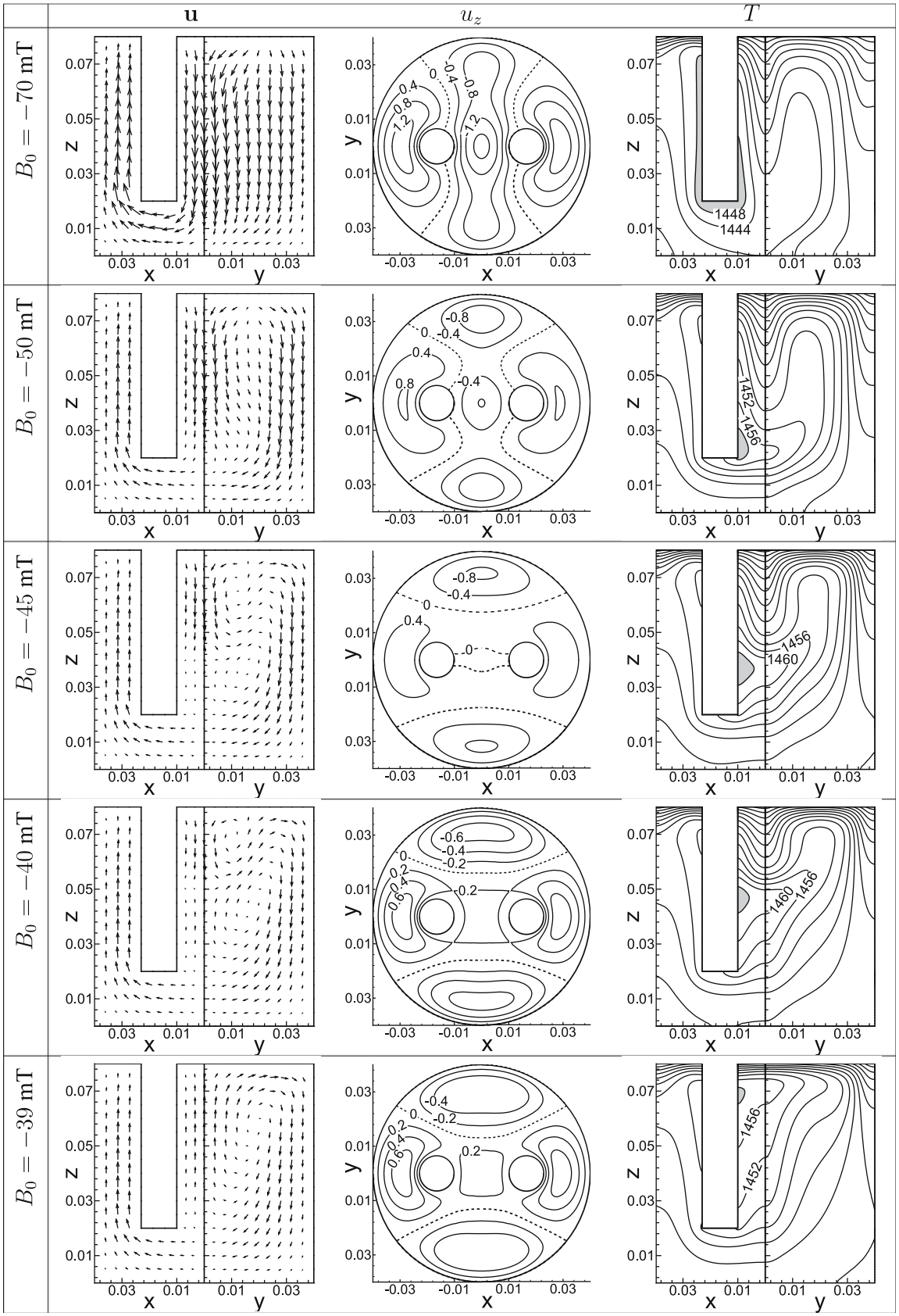

Fig. 11. Velocity and temperature distribution for a system with $U_E = 15$ V and stepwise increased B_0 ($B_0 = -70$ mT, -50 mT, -45 mT, -40 mT, -39 mT) starting with the converged solution for $B_0 = -71$ mT.

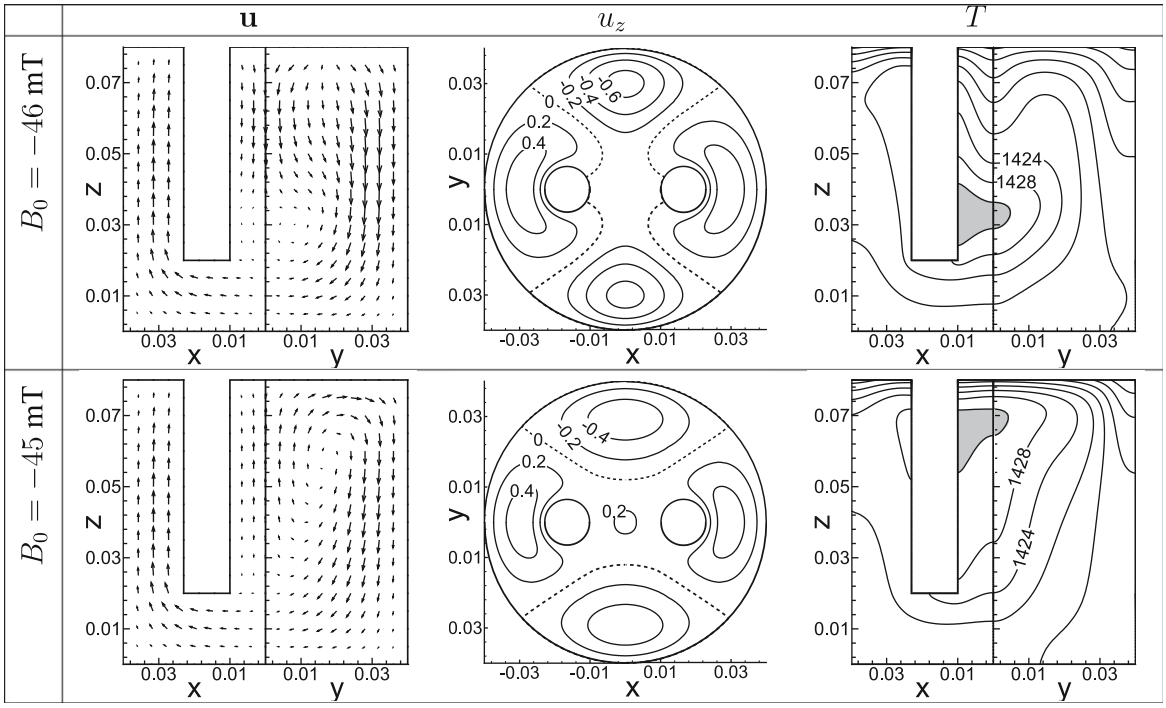

Fig. 12. Velocity and temperature distribution showing the transition from the lower to the upper branch of the hysteresis for $U_E = 12$ V.

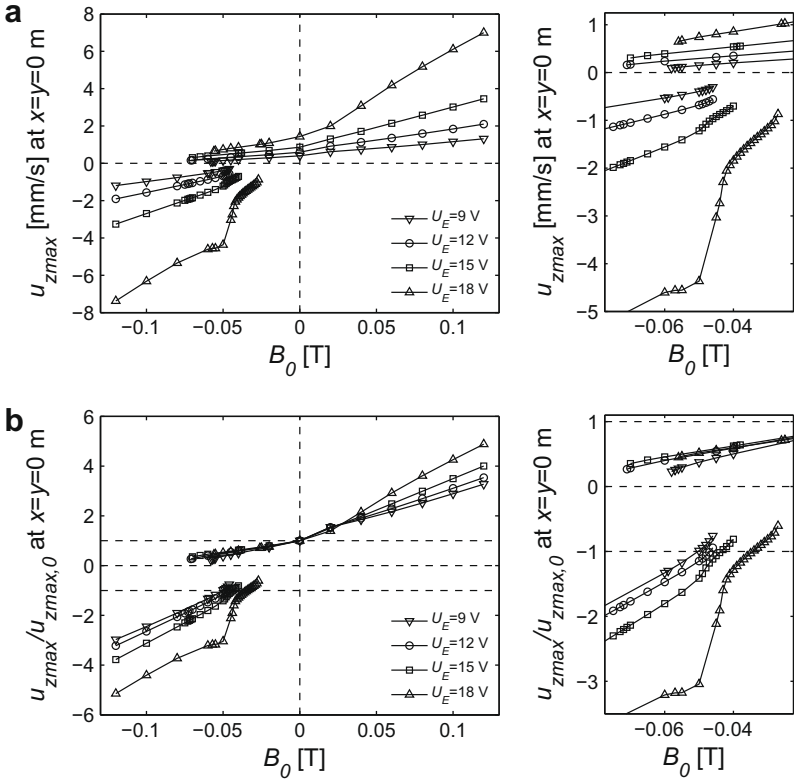

Fig. 13. (a) Maximum z-component of the velocity in the centerline of the crucible u_{zmax} as function of B_0 for various U_E. In (b) the ratio between u_{zmax} and $u_{zmax,0} = u_{zmax}(B_0 = 0\,\mathrm{T})$ is given. The detailed views (right) show that the range of two-valued solutions $u_{zmax}(B_0)$ depends significantly on U_E.

$\bar{u}$ is a linear function of B_0. Interestingly, in the linear regime with $B_0 < 0$ T the ratio $\bar{u}/\bar{u}_0$ is larger than for the same magnitude of B_0 with $B_0 > 0$ T. For example we have $\bar{u}/\bar{u}_0 \approx 4.5$ for $U_E = 18$ V, $B_0 = 120$ mT and $\bar{u}/\bar{u}_0 \approx 5$ for $U_E = 18$ V, $B_0 = -120$ mT. Before reaching the linear regimes (small magnitudes of B_0) buoyancy is still present and influencing the flow. The Lorentz force does not fully control the motion and hence, the slope of the graph $\bar{u}/\bar{u}_0(B_0)$ is smaller than in the linear regimes. Especially for $B_0 = -20$ mT the kinetic energy hardly increases as $1.00 \leqslant \bar{u}/\bar{u}_0 \leqslant 1.04$. If the flow pattern is identical to the Lorentz force

Table 3
Range of magnetic flux densities B_0 for which we obtain two different solutions depending on the starting conditions of the calculations. The range of B_0 varies with the electric potential difference U_E.

U_E (V)	Range of two-valued solution B_0 (mT)
9	−46 to −58
12	−46 to −71
15	−40 to −70
18	−27 to −56

distribution we can observe the linear relation between $\bar{u}$ and B_0. The right diagrams in Fig. 16 give detailed views of the two-valued regime. The discontinuous change of the flow pattern from $u_{zmax} > 0$ to $u_{zmax} < 0$ is reproduced by a discontinuous increase of $\bar{u}/\bar{u}_0(B_0)$ for all U_E. But the change from $u_{zmax} < 0$ to $u_{zmax} > 0$ results in a jump in the $\bar{u}/\bar{u}_0(B_0)$ graph only for $U_E = 9$ V and $U_E = 12$ V. The smooth transitions for $U_E = 15$ V and $U_E = 18$ V indicate that the kinetic energy in the system does not change during the change of the flow pattern.

The effect on the temperature and the temperature homogenization can be illustrated by the maximum temperature in the melt $T_{\max}$ and the difference of the maximum and minimum temperature in the melt

$$\Delta T = T_{\max} - T_{\min}. \tag{19}$$

In Fig. 17(a) $T_{\max}(B_0)$ and in Fig. 17(b) $\Delta T/\Delta T_0(B_0)$ with $\Delta T_0 = \Delta T(B_0 = 0\,\mathrm{T})$ are given. For $B_0 > 0$ T and all U_E we have $\Delta T/\Delta T_0 < 1$ which indicates that the temperature homogenization improves. The smaller U_E the smaller $\Delta T/\Delta T_0$ becomes. If we look at $B_0 < 0$ T and decrease B_0 starting from $B_0 = 0$ T we observe that ΔT significantly increases which indicates a worse temperature homogenization than without Lorentz force. For $U_E = 9$ V we have a maximum of $\Delta T/\Delta T_0 \approx 1.22$, but if we double U_E the maximum temperature difference in the melt is $\Delta T/\Delta T_0 \approx 1.73$ which is reached just before the change of flow direction. Also the transition from the lower to the upper branch of the hysteresis is characterized by $\Delta T/\Delta T_0 > 1$. The difference between $\Delta T/\Delta T_0$ of the various U_E is much larger for negative B_0 than for positive B_0, e.g. compare the results of $B_0 = -120$ mT with $B_0 = 120$ mT in Fig. 17(b). The reason might be the different locations of the temperatures hot spots each having different heat transport mechanism to the surrounding air with different cooling rates. After the change of flow direction for $B_0 < 0$ T hot fluid at the bottom of the electrodes cools down at the crucible wall. In contrast for $B_0 > 0$ T the hot fluid just below the surface is first cooled by radiative heat transfer. The heat flux at the crucible wall is approximately one order of magnitude smaller than the heat flux by radiation leading to a better cooling rate for $B_0 > 0$ T.

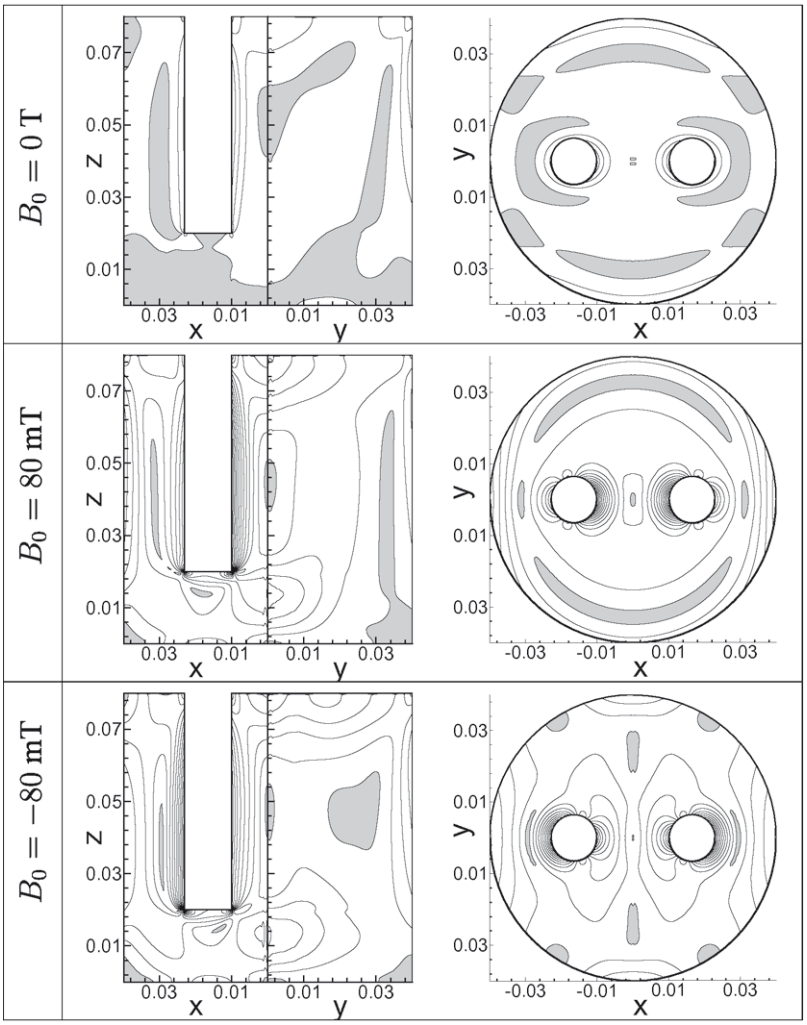

Fig. 14. Isolines of the maximum stretching function α in s^{-1} in the planes $y = 0$ m, $x = 0$ m (left) and $z = 0.04$ m for $U_E = 15$ V. In the first row α is given for pure thermal convection. The second ($B_0 = 80$ mT) and third row ($B_0 = -80$ mT) show α for Lorentz force dominated flows. The grey shading highlights areas with small values of the stretching function with $\alpha \leqslant 0.02\ s^{-1}$. Between the isolines the difference of α is $0.04\ s^{-1}$.

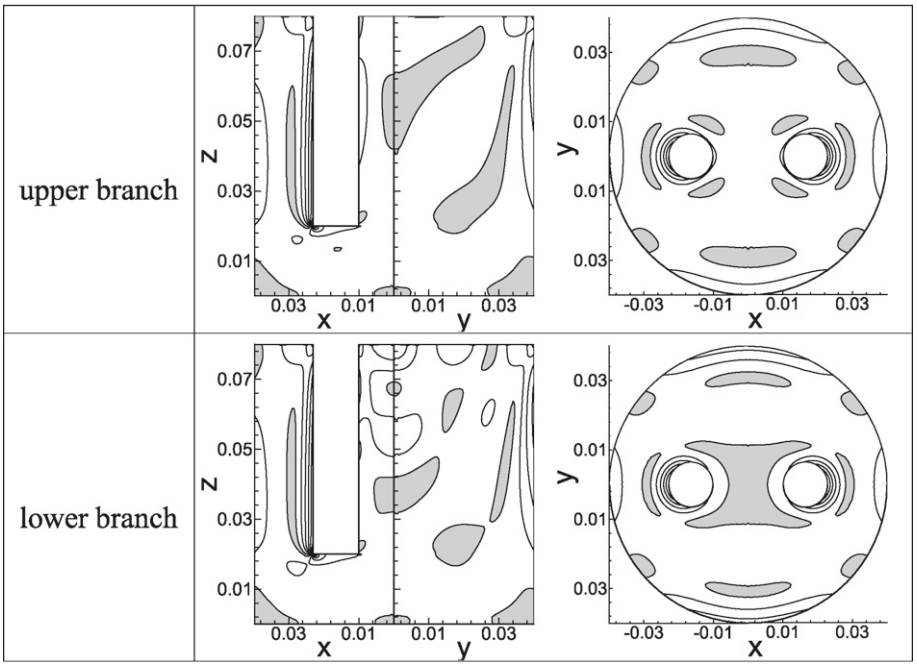

Fig. 15. Like in Fig. 14 the isolines of α are shown for $U_E = 15$ V. Here both plots are obtained for $B_0 = -40$ mT, whereas the first row belongs to the upper branch of the hysteresis with $u_{zmax} > 0$ and the second row belongs to the lower branch with $u_{zmax} < 0$.

Finally, let us have a look at the overall volume averaged Lorentz force

$$\bar{f}_L = V^{-1} \int (V) |\mathbf{f_L}| \, dV, \tag{20}$$

which is given in Fig. 18 as a function of B_0 for various U_E. First of all, for $B_0 > 0$ T and $U_E = 9$ V, 12 V, and 15 V $\bar{f}_L$ is almost linearly increasing with B_0. The parameters lead to a temperature range, in which the electrical conductivity is hardly changing with temperature. Therefore, the electric current density is almost independent of the flow – and $\bar{f}_L$ is a linear function of B_0. The impact of temperature-dependent electrical conductivity can be seen for $U_E = 18$ V and $B_0 > 0$ T. Here we have a larger temperature range, in which a reduction of T leads to a reduction of $\sigma(T)$ and **J**. As a result $\bar{f}_L$ slightly deviates from linearity. A deviation from linearity also exists in the parameter space in which we obtain two solutions. It can been seen already for $U_E = 12$ V, 15 V and is eyecatching for $U_E = 18$ V. Fig. 19 gives an answer to the question posed in the introduction:"Does the velocity depend linearly on the Lorentz force in a three-dimensional configuration as predicted by the one-dimensional analytical models?". The regions in which $\bar{u}/\bar{u}_0(\bar{f}_L)$ is almost a linear function are highlighted by the dashed straight lines. Again we identify two regions of linearity: for $B_0 > 0$ T shown in Fig. 19(a) and for solutions of the lower stable branch after the transition from the upper branch with $B_0 < 0$ T shown in Fig. 19(b).

5. Summary and conclusion

We have presented three-dimensional numerical studies of electromagnetically controlled thermal convection of glass melt in small scale crucible with two rod electrodes. The Lorentz force was imposed into the melt by the interaction of an external magnetic field with a constant density B_0 and an electric current density applied over the electrodes. During the simulations we varied the magnetic flux density between $-120\,\text{mT} \leqslant B_0 \leqslant 120\,\text{mT}$ and the electrode potential between $3\,\text{V} \leqslant U_E \leqslant 18\,\text{V}$.

The studies show that the Lorentz force leads to an overall increase of the kinetic energy in the system. For example for $B_0 = 120$ mT and $U_E = 18$ V the mean velocity is 4.5 times larger than without Lorentz force. Especially close to the bottom, a region

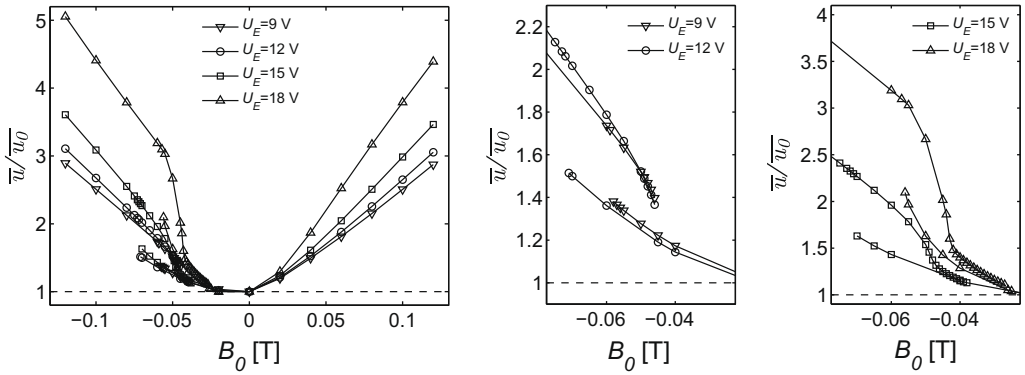

Fig. 16. Ratio $\bar{u}/\bar{u}_0$ as function of B_0 being a coarse global measure of the overall influence of the Lorentz force. The volume averaged velocity $\bar{u}$ is defined by $\bar{u} = \sqrt{\int |\mathbf{u}|^2 \, dV/V}$ and $\bar{u}_0 = \bar{u}(B_0 = 0\,\text{T})$ is the volume averaged velocity for pure thermal convection without Lorentz force. The Lorentz force increases the kinetic energy in the system, as $\bar{u}/\bar{u}_0 > 1$ for almost all $B_0 \neq 0$.

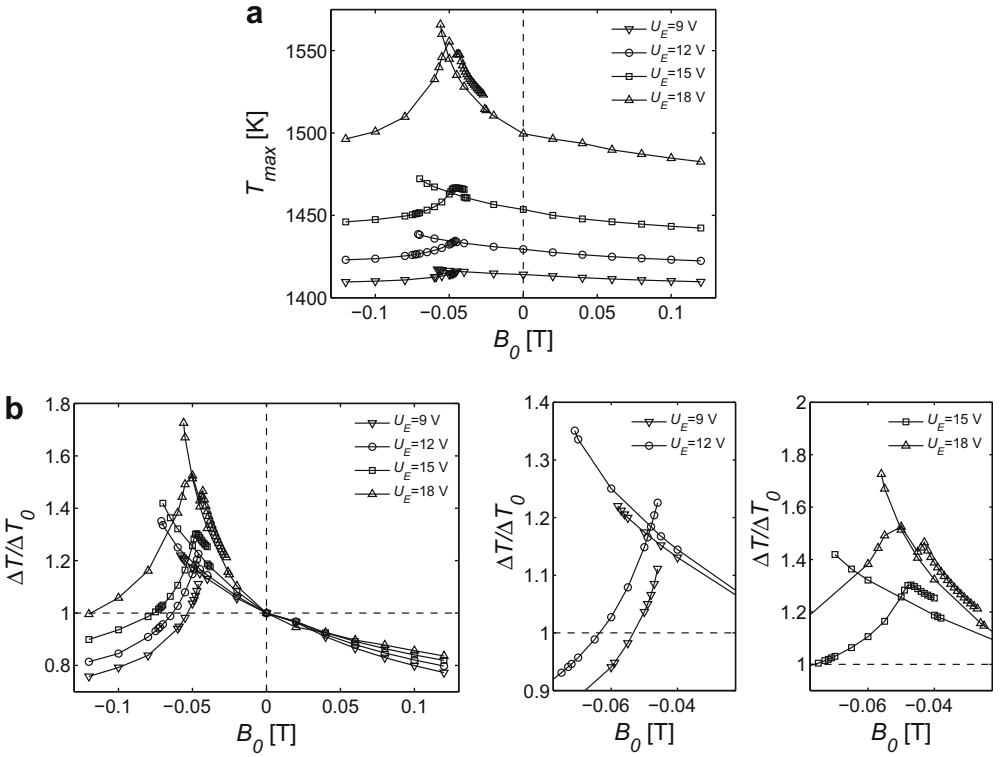

Fig. 17. (a) The maximum temperature in the melt T_{max} as function of B_0. In (b) the ratio of the temperature difference $\Delta T = T_{max} - T_{min}$ and the temperature difference of the pure thermal convection $\Delta T_0 = \Delta T(B_0 = 0\,\mathrm{T})$ is given. The temperature homogenization improves with B_0 if $\Delta T/\Delta T_0 < 1$ and changes to the worse for $\Delta T/\Delta T_0 > 1$.

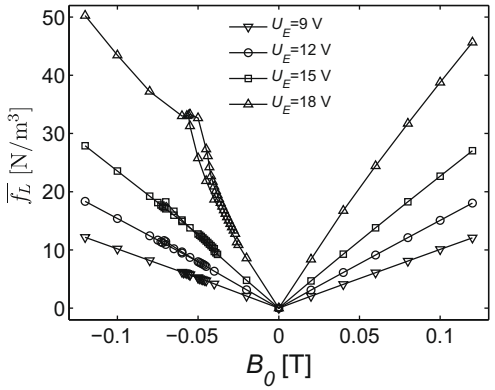

Fig. 18. Volume averaged Lorentz force $\bar{f}_L = V^{-1}\int|\mathbf{f_L}|\mathbf{dV}$ as function of the magnetic flux density B_0 for various electrode potentials U_E.

which is not affected by buoyancy, we observe a significant increase of the velocity. If the flow pattern is defined by the Lorentz force distribution, the mean velocity is a linear function of f_L. For $B_0 < 0\,\mathrm{T}$ the transition from a buoyancy dominated flow regime to a Lorentz force dominated one and vice versa is characterized by a discontinuous modification of the flow pattern between the electrodes. The transition to a Lorentz force dominated regime takes place for different B_0 than the transition to a buoyancy dominated regime. As a result we pass through a hysteresis and obtain two steady solutions for one set of parameters depending on the starting conditions. In this regime the maximum temperatures in the melt increase considerably and lead to a worsening of the temperature homogenization. Only for $B_0 > 0\,\mathrm{T}$ we observe an improvement of the temperature homogenization for all U_E.

The present model is given by the experimental studies of Krieger [20]. The dimensions of the setup are inspired by typical dimensions of forehearts and feeder systems. As we studied mag-

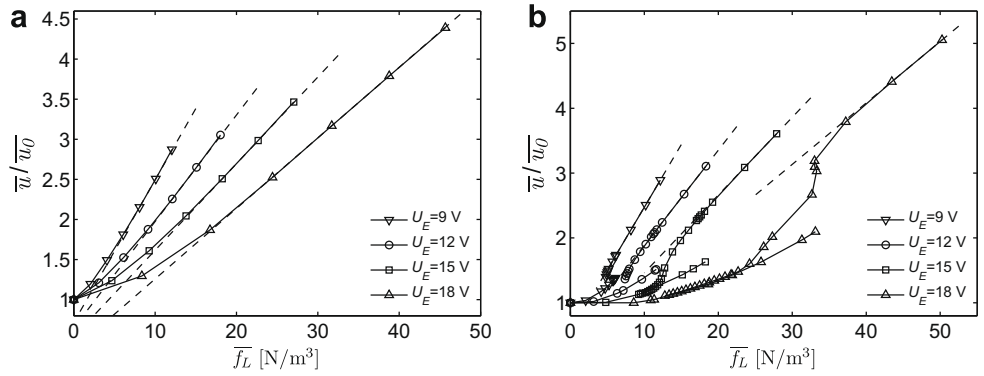

Fig. 19. The ratio $\bar{u}/\bar{u}_0$ as function of $\bar{f}_L$ for (a) $B_0 \geqslant 0\,\mathrm{T}$ and (b) $B_0 \leqslant 0\,\mathrm{T}$. It is a global but coarse indicator for how the Lorentz influences the kinetic energy. The dashed straight lines identify the regions in which $\bar{u}/\bar{u}_0(\bar{f}_L)$ is almost a linear function.

netic flux densities which are realizable in industrial applications, the present results can be used to estimate the effect on the flow with additional Lorentz forces. Even more, the significant results should be a motivation to move the establishment of electromagnetic flow control in glass processing forward. As the improvement of the homogeneity by Lorentz forces is an important measure it should be quantified more precisely in the future. Common is the statistical analysis of the deformation of particles, preferable length and surface stretch [31,9,33]. For this method the path of many particles has to be calculated. Time-dependent calculations would allow the application of higher constant electrical heat input q_{in}. Furthermore, one could investigate the impact of frequent variation of the B_0 sign – hence the f_L orientation. It is imaginable that the frequent variation of the B_0-direction will significantly improve the mixing rate as it is known from studies with mechanical stirrers. We have shown that the electric potential and hence, the electrode configuration define the Lorentz force distribution. Various parameter studies about the electrode configuration could give optimal setups which maximize the effect of the Lorentz force on the flow. Beside the studied top-electrode, side- and bottom-electrodes should be considered as well.

Acknowledgments

This work was supported by the Deutsche Forschungsgemeinschaft in frame of the Forschergruppe Magnetofluiddynamik. We are grateful to U. Lüdtke, U. Krieger, D. Hülsenberg and B. Halbedel for useful discussions. Especially we are grateful to H. Schwanbeck for technical support.

Appendix A. Estimation of the heat transfer coefficient *h*

The starting point for the estimation of the heat transfer coefficient h at the outer surface of the crucible wall is the laminar free convection on an isothermal vertical surface. For this case the Nusselt number

$$\mathrm{Nu} = \frac{hH}{\lambda_{\mathrm{air}}}, \tag{21}$$

a measure of the convective heat transfer, can be rewritten in terms of the Grashof number $\mathrm{Gr}_{\mathrm{air}}$ and an interpolation formula $g(\mathrm{Pr}_{\mathrm{air}})$ of the Prandtl number $\mathrm{Pr}_{\mathrm{air}}$ of the air outside the crucible according to [18]

$$\mathrm{Nu} = \frac{4}{3}\left(\frac{\mathrm{Gr}_{\mathrm{air}}}{4}\right)^{1/4} g(\mathrm{Pr}_{\mathrm{air}}). \tag{22}$$

If we assume a typical temperature difference between the crucible wall and the surrounding of 50 K and determine the air properties at the ambient temperature T_∞, we obtain a heat transfer coefficient of $h \approx 4\ \mathrm{W/m^2\,K}$.

References

[1] M.J. Austin, D.E. Bourne, A mathematical model of an electric glass furnace, Glass Technol. 14 (3) (1973) 78–84.
[2] D. Cepite, A. Jakovičs, B. Halbedel, U. Krieger, Modeling of electromagnetic glass convection with temperature-dependent properties of the melt, Magnetohydrodynamics 43 (2) (2007) 195–204.
[3] T.-S. Chen, R.E. Goodson, Computation of three-dimensional temperature and convective flow profiles for an electric glass furnace, Glass Technol. 13 (6) (1972) 161–167.
[4] M.K. Choudhary, A three-dimensional mathematical model for flow and heat transfer in electrical glass furnace, IEEE Trans. Ind. Gen. Appl. IA-22 (5) (1986) 912–921.
[5] M.K. Choudhary, A modeling study of flow and heat transfer in an electric melter, J. Non-Cryst. Solids 101 (1988) 41–53.
[6] R.L. Curran, Use of mathematical modeling in determining the effects of electrode configuration on convection currents in an electric glass melter, IEEE Trans. Ind. Gen. Appl. IGA-7 (1) (1971) 116–129.
[7] P.A. Davidson, Magnetohydrodynamics in materials processing, Annu. Rev. Fluid Mech. 31 (1999) 273–300.
[8] P.A. Davidson, An Introduction to Magnetohydrodynamics, Cambridge University Press, Cambridge, 2001.
[9] H. Eisermann, U. Lange, H. Loch, G. Weidmann, The intensity of mixing processes, in: D. Krause, H. Loch (Eds.), Mathematical Simulation in Glass Technology: Schott Series on Glass and Glass Ceramics, Springer, Berlin, 2002.
[10] Fluent Inc., FLUENT 6.3 Documentation, 2006.
[11] Fluent Inc., GAMBIT 2.3 Documentation, 2006.
[12] C. Giessler, U. Lange, A. Thess, Nonlinear laminar pipe flow of fluids with strongly temperature-dependent material properties, Phys. Fluids 19 (2007) 043601.
[13] C. Giessler, C. Sievert, U. Krieger, B. Halbedel, D. Hülsenberg, U. Lüdke, A. Thess, A model for electromagnetic control of buoyancy driven convection in glass melts, Fluid Dyn. Mater. Process. 1 (3) (2005) 247–266.
[14] C. Giessler, A. Thess, Analytical model of an electromagnetically controlled thermal fluid loop with strongly temperature-dependent material properties, J. Fluid Mech. 618 (2009) 135–154.
[15] B. Halbedel, D. Hülsenberg, U. Krieger, U. Lüdtke, G. Carl, H.-J. Linz, Methode and device for electromagnetically influencing the flow conditions in fluids of low electrical conductivity and high viscosity, WO 2007 065 937, 2007.
[16] T. Hiemjima, H. Azuma, M. Sawasaki, Numerical analysis and measurement of glass flow in a small melting furnace, Glass Sci. Technol. 76 (4) (2003) 155–165.
[17] D. Hülsenberg, B. Halbedel, G. Conrad, A. Thess, Y. Kolesnikov, U. Lüdtke, Electromagnetic stirring of glass melts using Lorentz forces – experimental results, Glass Sci. Technol. 77 (2004) 186–193.
[18] F.P. Incropera, D.P. DeWitt, Fundamentals of Heat and Mass Transfer, Wiley, Berlin, 1996.
[19] J.D. Jackson, Classical Electrodynamics, Wiley, Berlin, 1975.
[20] U. Krieger. Einfluss elektromagnetisch generierter Kraftwirkungen auf die Strömungen in Glasschmelzen, Ph.D. Thesis, TU Ilmenau, 2007 (in German).
[21] U. Krieger, B. Halbedel, D. Hülsenberg, A. Thess, Electromagnetic control of the glass melt flow in crucibles, Eur. J. Glass Sci. Technol. A 49 (1) (2008) 33–40.
[22] R. Krishnamurti, On the transition to turbulent convection. Part 1. The transition from two- to three-dimensional flow, J. Fluid Mech. 42 (1970) 295–307.
[23] R. Krishnamurti, On the transition to turbulent convection. Part 2. The transition to time-dependent flow, J. Fluid Mech. 42 (1970) 309–320.
[24] F.A. Kulacki, R.J. Goldstein, Thermal convection in a horizontal fluid layer with uniform volumetric energy sources, J. Fluid Mech. 55 (2) (1972) 271–287.
[25] C. Kunert, A. Langsdorf, F. Lentes, K. Duch, A. Thess, Y. Kolesnikow, Verfahren und Anordnung zur Zufuhr einer Glasschmelze zu einem Verarbeitungsprozess, DE 10 2004 015 055, 2004 (in German).
[26] L. Mardorf, G. Woelk, Berechnung des Verhaltens einer elektrisch beheizten Glasschmelzwanne mit einem mathematischen Modell, Glastech. Ber. 54 (4) (1983) 73–84 (in German).
[27] A.E. Mikelson, V.N. Moshnyaga, A.D. Osmanis, V.T. Slavyanskij, V.S. Shashkin, Methode of glass melting, SU 814904, 1981 (in Russian).
[28] G. Nölle, Technik der Glasherstellung, Deutscher Verlag für Grundstoffindustrie, 1997 (in German).
[29] A.D. Osmanis, A.K. Snijedze, A.M. Aglitis. Influence of electromagnetic stirring of glass melts, in: Proceedings of the 12th Riga Symposium on Magnetohydrodynamics, Salaspils, USSR, 1987, pp. 179–183 (in Russian).
[30] A.D. Osmanis, A.E. Mikelson, L.Y. Pochs, I. Barbans, O.M. Mezhdrejs, V.V. Troshin, V.I. Butaeva, N.M. Vygorka, A.I. Grigorev, V.M. Zalevskij, Methode of glass melting, SU 1024423, 1983 (in Russian).
[31] J.M. Ottino, The Kinematics of Mixing: Stretching Chaos and Transport, Cambridge University Press, Cambridge, 1989.
[32] R. Schumacher, Stabilitätsprobleme beim Widerstandsheizen von Glasschmelzen, Glastech. Ber. 55 (12) (1982) 243–248 (in German).
[33] S. Schütz, Berechnung und Analyse der Vermischung von Flüssigkeiten im Makro- und Mikromaßstab bei laminarer Strömung, Shaker, 2006 (in German).
[34] H.-U. Seidel, Zu einigen Fragen des vollelektrischen Schmelzens von Gläsern mittels elektrischer Widerstandsbeheizung, Ph.D. Thesis, TU Ilmenau, 1977 (in German).
[35] W. Trier, Glasschmelzöfen, Springer, Berlin, 1984 (in German).
[36] E. Truckenbrodt, Fluidmechanik, Band 2, Springer, Berlin, 1992 (in German).
[37] A. Ungan, R. Viskanta, Three-dimensional numerical simulation of circulation and heat transfer in an electrically boosted glass melting tank, IEEE Trans. Ind. Appl. IA-22 (5) (1986) 922–933.
[38] A. Ungan, R. Viskanta, Three-dimensional numerical modeling of circulation and heat transfer in a glass melting tank. Part 1. Mathematical formulation, Glastech. Ber. 60 (3) (1987) 71–78.
[39] A. Ungan, R. Viskanta, Three-dimensional numerical modeling of circulation and heat transfer in a glass melting tank. Part 2. Sample simulations, Glastech. Ber. 60 (4) (1987) 115–124.
[40] A.J. Walkden, Improvements in or relating to the manufacture of glass, GB 1289317, 1972.